



Large-scale hydrologic and hydrodynamic modelling of the Amazon River basin

Rodrigo Paiva, Diogo Buarque, Walter Collischonn, Marie-Paule Bonnet, Frédéric Frappart, Stéphane Calmant, Carlos Mendes

► To cite this version:

Rodrigo Paiva, Diogo Buarque, Walter Collischonn, Marie-Paule Bonnet, Frédéric Frappart, et al.. Large-scale hydrologic and hydrodynamic modelling of the Amazon River basin. Water Resources Research, American Geophysical Union, 2013, 49 (3), pp.1226-1243. <10.1002/wrcr.20067>. <hal-00873165>

HAL Id: hal-00873165

<https://hal.archives-ouvertes.fr/hal-00873165>

Submitted on 15 Oct 2013

HAL is a multi-disciplinary open access archive for the deposit and dissemination of scientific research documents, whether they are published or not. The documents may come from teaching and research institutions in France or abroad, or from public or private research centers.

L'archive ouverte pluridisciplinaire **HAL**, est destinée au dépôt et à la diffusion de documents scientifiques de niveau recherche, publiés ou non, émanant des établissements d'enseignement et de recherche français ou étrangers, des laboratoires publics ou privés.

1
2
3
4
5
6
7
8
9
10
11
12
13
14
15
16
17
18
19
20
21

Large-scale hydrologic and hydrodynamic modelling of the Amazon River basin

Rodrigo Cauduro Dias de Paiva^{1,2}

Diogo Costa Buarque¹

Walter Collischonn¹

Marie-Paule Bonnet²

Frédéric Frappart²

Stephane Calmant³

Carlos André Bulhões Mendes¹

¹ Instituto de Pesquisas Hidráulicas IPH, Universidade Federal do Rio Grande do Sul
UFRGS, Porto Alegre, Brazil.

² Université Toulouse III Paul Sabatier, OMP, GET (UMR 5563 CNRS IRD UPS)
Toulouse, France.

³ Université Toulouse III Paul Sabatier, OMP, LEGOS (UMR 5566 CNES CNRS IRD
UPS) Toulouse, France.

rodrigodpaiva@gmail.com

* Corresponding author

Abstract

In this paper, a hydrologic/hydrodynamic modelling of the Amazon River basin is presented using the MGB-IPH model with a validation using remotely-sensed observations. Moreover, the sources of model errors by means of the validation and sensitivity tests are investigated and the physical functioning of the Amazon basin is also explored. The MGB-IPH is a physically-based model resolving all land hydrological processes and here using a full 1D river hydrodynamic module with a simple floodplain storage model. River-floodplain geometry parameters were extracted from SRTM DEM and the model was forced using satellite-derived rainfall from TRMM3B42. Model results agree with observed *in situ* daily river discharges and water levels and with three complementary satellite-based products: (i) water levels derived from ENVISAT altimetry data; (ii) a global dataset of monthly inundation extent; and (iii) monthly terrestrial water storage (TWS) anomalies derived from GRACE. However, the model is sensitive to precipitation forcing and river-floodplain parameters. Most of the errors occur in westerly regions, possibly due to the poor quality of TRMM 3B42 rainfall dataset in these mountainous and/or poorly monitored areas. Also, uncertainty in river-floodplain geometry causes errors in simulated water levels and inundation extent, suggesting the need for improvement of parameter estimation methods. Finally, analyses of Amazon hydrological processes demonstrate that surface waters governs most of the Amazon TWS changes (56%), followed by soil water (27%) and ground water (8%). Moreover, floodplains play a major role in stream flow routing, although backwater effects are also important to delay and attenuate flood waves.

47 **Keywords:** large-scale hydrologic hydrodynamic model, Amazon, flood inundation,
48 remote sensing, MGB-IPH, GRACE, ENVISAT radar altimetry, Amazon hydrological
49 processes
50

51 **1. Introduction**

52

53 The development of large-scale hydrological models has been a subject of
54 important research topics in the past decades. These models, when used in forecast
55 systems, may help reducing population vulnerability to natural hazards, particularly in
56 the Amazon River basin, where extreme hydrological events have occurred in the past
57 few years, such as the floods of 2009 and 2012 and the droughts in 1996, 2005 and 2010
58 (*Chen et al.*, 2010; *Tomasella et al.* 2010; *Marengo et al.*, 2008; *Espinoza et al.*, 2011,
59 *Marengo et al.*, 2011). Furthermore, complementary to observational studies (*e.g.*
60 *Frappart et al.*, 2011a; *Azarderakhsh et al.*, 2011; *Alsdorf et al.*, 2007a), simulation
61 models can support the understanding and quantification of different Amazon
62 hydrological processes such as evapotranspiration, soil and groundwater storages and
63 river-floodplain hydrodynamics (*e.g.* *Costa and Foley*, 1997; *Trigg et al.* 2009).

64 Part of recent model developments concerns river and floodplain flow, which is
65 an important factor in the Amazon hydrology. *Trigg et al.* (2009) showed that the
66 Amazon flood wave is subcritical and diffusive. Consequently, backwater effects cause
67 the influence of sea tides on the main river channel to be perceived more than ~1000 km
68 upstream the river mouth (*Kosuth et al.*, 2009). It also causes the influence of the main
69 river over its tributaries (*Meade*, 1991) and controls droughts (*Tomasella et al.*, 2010).
70 Floodplain inundation is also an important issue (*Bonnet et al.*, 2008; *Alsdorf et al.*,
71 2007a; and *Alsdorf et al.*, 2010), playing a significant role in large-scale flood
72 propagation (*Paiva et al.*, 2011b; *Yamazaki et al.*, 2011), in sediment dynamics
73 (*Bourgoin et al.*, 2007), in chemical and ecological conditions (*Junk*, 1997, *Richey et*
74 *al.*, 2002, *Melack et al.*, 2004, *Seyler and Boaventura*, 2003 among others) and in the

75 climate system due to land surface and atmosphere interactions (*Mohamed et al.*, 2005;
76 *Paiva et al.*, 2011c; *Prigent et al.*, 2011).

77 Recent modelling developments used different kinds of approaches aiming at
78 sufficiently representing physical processes, but considering computational and input
79 data limitations. River hydrodynamics are generally represented by simplifications of
80 *Saint Venant* equations, including a simplistic relation between water volume storage
81 and discharge (e.g. *Coe et al.*, 2008), kinematic wave models (*Decharme et al.* 2011;
82 *Getirana et al.* 2012) or Muskingum Cunge type methods (*Collischonn et al.*, 2008;
83 *Beighley et al.*, 2009); diffusive wave models (*Yamazaki et al.*, 2011) or a full
84 hydrodynamic model (*Paiva et al.*, 2011a; *Paiva et al.*, 2012) where only the last two
85 can represent the aforementioned backwater effects. Although the use of hydrodynamic
86 models within large-scale distributed hydrological models is still uncommon, they also
87 have been applied in other relatively large-scale problems (*Paz et al.*, 2010;
88 *Biancamaria et al.*, 2009; *Lian et al.*, 2007). When included, floodplain flows are
89 modelled by different approaches: assuming storage areas having the same river water
90 levels (e.g. *Paiva et al.*, 2011a; *Paiva et al.*, 2012; *Yamazaki et al.*, 2011) or considering
91 water exchanges between river and floodplains as a function of river-floodplain water
92 slope (e.g. *Decharme et al.* 2011); adopting a composed river floodplain cross sections
93 with 1D floodplain flow (e.g. *Beighley et al.*, 2009; *Getirana et al.*, 2012); or
94 considering 2 D floodplain flows (e.g. *Wilson et al.*, 2007; *Trigg et al.*, 2009). In most
95 of the cases, river bathymetry is approximated by a rectangular shape with parameters
96 estimated as function of the upstream drainage area (or mean discharge) using empirical
97 relations. Digital Elevation Models such as the SRTM DEM (*Farr et al.*, 2007) are used
98 to estimate floodplain bathymetry and river bottom level or surface water slope. Model
99 limitations can be due to the simplifications on representing physical processes but also

100 due to the deficiencies on the aforementioned input data. Consequently, model
101 validations and investigations of the source of errors may guide the improvement of
102 current models.

103 In this direction, additionally to *in situ* data commonly used for validation,
104 remote sensing-derived hydrological datasets, such as river stages based on satellite
105 altimetry measurements (*Alsdorf et al., 2007b; Santos da Silva et al., 2010*), inundation
106 extent (*e.g. Hess et al., 2003; Papa et al., 2010*) or Terrestrial Water Storage (TWS)
107 derived from the GRACE gravimetry from space mission (*Tapley et al., 2004*), offer a
108 new opportunity to compare and validate simulation outputs and improve these
109 hydrological modelling approaches.

110 In this study, we present a hydrologic/hydrodynamic modelling of the Amazon
111 River basin using the MGB-IPH hydrological model (“*Modelo de Grandes Bacias*”,
112 *Collischonn et al., 2007*) with a full river hydrodynamic module coupled with a simple
113 floodplain storage model (*Paiva et al., 2011a*) validated against remotely-sensed
114 observations. We first present an extensive model validation based on comparisons
115 between model outputs and i) *in situ* stream stages and discharges and also water levels
116 derived from ENVISAT RA-2 satellite altimetry data from *Santos da Silva et al. (2010)*;
117 ii) monthly inundation extent from a multisatellite product (*Papa et al., 2010*); and (iii)
118 GRACE-based TWS from *Frappart et al. (2010; 2011b)*. Then, using the validation
119 results and also sensitivity analyses, we determine the source of model errors in the
120 Amazon, that may be extrapolated to other similar large-scale hydrological models
121 Finally, the hydrological functioning of the Amazon River basin is explored using the
122 model results, including aspects such as water balance, the surface, soil and ground
123 water partitioning and the role of river-floodplain hydraulics on stream flow routing.

124

125

126 **2. Methods and datasets**

127

128 2.1. The Hydrologic-Hydrodynamic Model

129

130 The MGB-IPH model is a large-scale distributed hydrological model that uses
131 physical and conceptual equations to simulate land surface hydrological processes
132 (*Collischonn et al.* 2007). It uses a catchment-based discretization and the hydrological
133 response units (HRUs) approach. The simulated vertical hydrological processes include
134 soil water budget using a bucket model, energy budget and evapotranspiration using
135 Penman Monteith approach, interception and soil infiltration, surface runoff based on
136 the variable contributing area concept and also subsurface and groundwater flow
137 generation. The flow generated within the HRUs of each catchment is routed to the
138 stream network using three linear reservoirs representing the groundwater, subsurface
139 and surface flow. River flow routing is performed using a combination of either a
140 Muskingum-Cunge (MC) method or a hydrodynamic model (HD).

141 The large-scale hydrodynamic model of MGB-IPH was developed by *Paiva et*
142 *al.* (2011a) and applied to the Solimões River basin by *Paiva et al.* (2012). This model
143 differs from the MC model by its capacity to simulate flood inundation and backwater
144 effects. The model solves the full 1-D *Saint-Venant* equations (*Cunge et al.*, 1980) for a
145 river network using an implicit finite difference numeric scheme and a Gauss
146 elimination procedure based on a modified skyline storage method. Flood inundation is
147 simulated using a simple storage model (*Cunge et al.*, 1980), assuming that (i) the flow
148 velocity parallel to the river direction is null on the floodplain, (ii) the floodplains act
149 only as storage areas, (iii) the floodplain water level equals the water level at the main

150 channel. Consequently, the river-floodplain lateral exchange equals $q_{fl} = (dz/dt)A_{fl}(z)/dx$
151 where x and t are spatial and time dimensions and z is the river water level, and $A_{fl}(z)$ is
152 the flooded area inside a floodplain unit as described below. GIS-based algorithms are
153 used to extract river and floodplain geometry parameters mainly from Digital Elevation
154 Models (DEM) (Paiva et al., 2011a). Parameters from a rectangular-shaped river cross
155 section are estimated using geomorphologic equations and the river bottom level is
156 estimated from the DEM using corrections presented in Paiva et al. (2011a). The
157 algorithm delineates discrete “floodplain units” for each sub-reach and extracts a z vs
158 A_{fl} curve from the DEM for each of them. Corrections are applied on the DEM since
159 SRTM signal does not penetrate vegetation or surface water and consequently does not
160 provide ground elevation. Flood inundation results in terms of 2D water levels are
161 computed based on 1D water level outputs and the DEM.

162

163

164 2.2. The Amazon River basin

165

166 The Amazon River basin (Fig. 1a) is known as the world’s largest river basin. It
167 has 6 million km² of surface area and drains ~15% of the total amount of fresh water
168 dumped into oceans. This region exhibits high rainfall rates (average ~2200 mm/year)
169 with high spatial variability (Espinoza et al., 2009a). Contrasting rainfall regimes are
170 found in northern and southern parts of the basin, with the rainy season happening on
171 June, July and August (on December, January and February) in the North (South) with
172 more (less) defined wet and dry seasons occurring in the southern and eastern (northern
173 and western) parts of the basin (Espinoza et al., 2009a). The Amazon basin is composed
174 by three morphological units: the Andes with high altitudes and slopes, the Guyanese

175 and Brazilian shields with moderate slopes and the Amazon plain with very low slopes.
176 Extensive seasonally flooded areas are found at the Amazon plains (*Hess et al.*, 2003;
177 *Papa et al.*, 2010). Also, this region is characterized by complex river hydraulics, where
178 the low river slopes cause backwater effects to control part of the river dynamics
179 (*Meade*, 1991; *Paiva et al.*, 2012). The abovementioned characteristics put together give
180 rise to an interesting discharge regime. Rivers draining southern areas have a maximum
181 flow occurring from March to May and a minimum one from August to October
182 (*Espinoza et al.*, 2009a). In some other rivers a weaker seasonal regime can be found, in
183 some cases due to rainfall characteristics and in others, such as the Solimões/Amazon
184 main stem, due to the contribution of lagged hydrographs from northern and southern
185 areas. In the latter, high (low) water occurs generally from May to July (September to
186 November).

187

188 2.3. Model discretization, parameter estimation and forcing data.

189

190 The model discretization into river reaches, catchments, hydrodynamic
191 computational cross sections and parameter estimation was carried out using the SRTM
192 DEM (*Farr et al.*, 2007) with 15" resolution (~ 500 m) (see Fig. 1a) and GIS based
193 algorithms described in *Paiva et al.* (2011a). The Amazon basin was discretized into
194 5763 catchments, ranging from 100 to 5000 km² (Fig. 1b).

195 An HRU map with 12 classes was developed using Brazilian and South
196 American soil and vegetation maps (*RADAMBRASIL*, 1982; *Dijkshoorn et al.*, 2005;
197 *Eva et al.*, 2002), and the Height Above the Nearest Drainage (HAND) terrain
198 descriptor (*Rennó et al.*, 2008) to identify areas close to rivers where plant-groundwater
199 interactions might take place.

200 To avoid excessive computing time, we used a combination of the Muskingum
201 Cunge (MC) and hydrodynamic (HD) models (Fig. 1c). River reaches which were
202 simulated with the HD model were selected using the following criteria: (i) river slope
203 lower than 20cm/km, based on *Ponce's* (1989) criteria for kinematic wave models and
204 (ii) presence of large floodplains using DEM visual inspection. As a result, ~30% of the
205 reaches were simulated using the HD model (Fig. 1c). River reaches were then
206 discretized considering the distance between two computational cross sections
207 $\Delta x = 10$ km, based on the criteria of the hydrodynamic model numerical scheme
208 performance (*Castellarin et al.*, 2009; *Cunge et al.*, 1980; *Paiva et al.*, 2011a).
209 Temporal discretization for both HD and MC models were $\Delta t = 3600$ s, based on
210 Courant criteria (*Cunge et al.*, 1980).

211 River geometry parameters, i.e. river width B [m] and maximum water depth H
212 [m], were estimated as a function of the drainage area Ad [km²], using geomorphologic
213 equations developed from river cross sections surveys achieved at stream gauge
214 locations provided by the Brazilian Water Resources Agency (ANA). We developed
215 different sets of geomorphologic equations for six sub-basins within the Amazon
216 defined by its major tributaries, as shown in Table 1 (also see Fig. 1a).

217 River bottom levels were estimated from the DEM using *Paiva et al.* (2011a)
218 algorithms and $H_{veg} = 17$ m (vegetation height) to eliminate DEM errors due to
219 vegetation. Also, when using DEM to extract water level vs flooded area curves, all of
220 its pixel values (Z_{DEM}) were corrected using $Z_{DEM}^* = Z_{DEM} - H_{veg}$, except for areas with
221 low vegetation, according to the HRU map.

222 Meteorological data were obtained from the CRU CL 2.0 dataset (*New et al.*,
223 2002), which provides monthly climatological values calculated using interpolated data
224 from ground stations for the period between 1960 and 1990 at a spatial resolution of

225 10', which is in accordance with the low density of meteorological stations in the
226 Amazon. We also used TRMM daily precipitation data provided by algorithm 3B42
227 (*Huffman et al.*, 2007), with a spatial resolution of $0.25^{\circ} \times 0.25^{\circ}$ for the 12-year period
228 1998–2009.

229 The MGB-IPH model parameters related to soil water budget were calibrated
230 against discharge data from stream gauges using the MOCOM-UA optimization
231 algorithm (*Yapo et al.*, 1998; *Collischonn et al.*, 2007) for the 1998-2005 time period,
232 using the model performance statistics E_{NS} , E_{NSlog} and ΔV , described in the next section.
233 For parameter calibration, model runs were used only within the MC model to avoid
234 high computational costs and, therefore, we used only stream gauges located in river
235 reaches simulated with the MC model (Fig. 1c). Gauges located in reaches simulated
236 with the HD model were used only for validation. The calibration procedure optimized
237 6 parameters related to soil water budget for each HRU (the maximum water storage in
238 the upper layer of soil W_m ; 3 equivalent hydraulic conductivities K_{bas} , K_{int} , K_{cap} ; the
239 parameter from the variable contributing area model for runoff generation b), and 3
240 parameters related to surface, subsurface and base flow residence time (C_s , C_i and
241 TKB), following *Collischonn et al.* (2007). We optimized these parameters for each
242 large river sub-basin, giving rise to tens of different parameter sets with the following
243 median values and ranges (5% and 95% percentiles): $W_m = 282$ (30-1800) mm, $b =$
244 0.48 (0.02-4.6), $K_{bas} = 1.2$ (0.03-6.9) mm/day, $K_{int} = 5.2$ (0.2-200) mm/day, $K_{cap} =$
245 0.02 (0-0.26) mm/day, $C_s = 12.4$ (5.6-35.5), $C_i = 10.0$ (3.9-1379), $TKB = 99$ (18-386)
246 days. In some cases (10%), calibrated parameters were out of these ranges, possibly due
247 to input data errors (e.g. precipitation as discussed later) or even limitations in the
248 model. Vegetation parameters used in energy balance and evapotranspiration
249 computations (e.g. leaf area index, superficial resistance, albedo and vegetation height)

250 were taken from *Shuttleworth* (1993). The only parameter related to the hydrodynamic
251 model is the Manning's coefficient and it was not calibrated using the MOCOM-UA
252 algorithm. Instead, we used different values for different large river basins aiming at
253 fitting hydrographs in the largest Amazonian rivers (0.035 in almost all the Amazon
254 basin, 0.025 in the lower Madeira basin, 0.030 in the upper Madeira, upper Solimões
255 and upper Negro basins, 0.040 in upper part of Brazilian Solimões River).

256

257 2.4. Model validation approach

258

259 Discharge

260

261 Daily discharge results were compared with data from 111 stream gauges (Fig.
262 2) provided by the Brazilian Agency for Water Resources ANA (Agência Nacional das
263 Águas), the Peruvian and Bolivian National Meteorology and Hydrology Services
264 SENAMHI (Servicio Nacional de Meteorología e Hidrología) and the Hydrology,
265 Biogeochemistry and Geodynamic of the Amazon Basin (HYBAM) program
266 (<http://www.ore-hybam.org>) for the 1999-2009 period. Values from the HYBAM
267 database provided better discharge estimates in the central Amazon since it is based on
268 both stages and water slope and, consequently, are able to represent looped rating
269 curves.

270

271 Water level

272

273 Simulated daily water levels were validated against stream gauge records and
274 radar altimetry data. We used 69 stream gauges for the 1998-2005 period, selected from
275 ANA's database (see Fig. 5).

276 We also compared the computed water levels with ENVISAT satellite altimetry
277 data. ENVISAT satellite has a 35-day repeat orbit and an 80 km inter-track distance.
278 The database used is an extension of the one presented in *Santos da Silva et al. (2010)*.
279 It consists of 212 altimetry stations (AS – deduced from the intersection of a satellite
280 track with a water body) with water level time series reported to EGM08 geoid for the
281 2002-2009 period. Altimetry stations are located mainly along the Solimões, Amazon,
282 Juruá, Japurá, Madeira, Negro and Branco Rivers (see Fig. 5). ENVISAT data selection
283 techniques preconized by *Santos da Silva et al. (2010)* result in ~ 10 to 40 cm water
284 level accuracy. Since water level model results are based on the SRTM DEM, it became
285 necessary to convert ENVISAT water levels from their initial EGM08 geoidal reference
286 to an EGM96 geoidal reference. We used the programs provided by the National
287 Geospatial-Intelligence agency (<http://earth-info.nga.mil/>) to perform the conversion.

288

289

290 Flood Extent

291

292 Flood inundation results were compared to a multi-satellite monthly global
293 inundation extent dataset at a ~25 x 25 km spatial resolution and available over the 1993
294 to 2004 period (*Papa et al., 2010*). This product was derived from multiple-satellite
295 observations, including passive (Special Sensor Microwave Imager) and active (ERS
296 scatterometer) microwaves along with visible and near-infrared imagery (advanced very
297 high-resolution radiometer; AVHRR). This dataset was already used for validating other

298 large-scale streamflow routing and flood models (e.g. *Decharme et al.*, 2011; *Yamazaki*
299 *et al.*, 2011). It is provided on an equal area grid of $0.25^{\circ} \times 0.25^{\circ}$ at the Equator where
300 each pixel has 773km^2 of surface area. Considering this, for model validation, we
301 computed daily water depth grids at a 15" resolution (~ 500 m) based on simulated water
302 levels and the DEM, as described in *Paiva et al.* (2011a), and then we resampled it into
303 a $\sim 25 \times 25$ km grid to compute monthly inundation extent only for the 1999-2004 time
304 period.

305

306 Terrestrial water storage

307

308 The Gravity Recovery and Climate Experiment (GRACE) mission, launched in
309 March 2002, provides measurements of the spatio-temporal changes in Earth's gravity
310 field. Several recent studies have shown that GRACE data over the continents can be
311 used to derive the monthly changes of the terrestrial water storage (TWS) (*Ramillien et*
312 *al.*, 2005 and 2008; *Schmidt et al.*, 2008) with an accuracy of ~ 1.5 cm of equivalent
313 water thickness when averaged over surfaces of thousands of square-kilometres. These
314 TWS changes estimates over land include all hydrological compartments, such as rivers,
315 floodplains, lakes, soil and groundwater. We used the Level-2 land water solutions
316 (RL04) produced by GFZ, JPL, and CSR with a spatial resolution of ~ 333 km, and an
317 accuracy of 15-20 mm of water thickness. These are smoothed solutions using a 400
318 and 500 km halfwidth Gaussian filter and provided at $1 \times 1^{\circ}$ and at a monthly time
319 interval. They are also post-processed using an Independent Component Analysis (ICA)
320 approach (*Frappart et al.*, 2010) which demonstrates a strong capacity for removing the
321 north-south stripes polluting the GRACE solutions (*Frappart et al.*, 2011b).

322 To derive TWS estimates from the MGB-IPH model we used the following
323 procedure. For each catchment, total water storage S (considering river, floodplain,
324 surface, soil and ground waters) is related to precipitation (P), evapotranspiration (ET),
325 river inflow (I) and outflow (O) by the continuity equation $dS/dt = (P - ET).A_d + I - O$,
326 where A_d is the catchment drainage area and t is time. For each day, water storage was
327 derived as $S_{t+1} = S_t + [(P_{t,t+1} - ET_{t,t+1}).A_d + I_{t,t+1} - O_{t,t+1}]\Delta t$ where Δt is the time
328 interval, similarly as used by *Getirana et al.* (2011) at the basin scale for the Negro
329 River basin.

330 Then, to derive model TWS estimates comparable with GRACE data, we
331 smoothed MGB-IPH TWS values using a 450 km halfwidth Gaussian filter. Moreover,
332 since the original GRACE spatial resolution is larger than $1^\circ \times 1^\circ$, we chose to resample
333 both GRACE and MGB-IPH data to a $4^\circ \times 4^\circ$ grid (Fig. 9). For each $4^\circ \times 4^\circ$ pixel, TWS
334 derived from GRACE was computed as a simple average of the $1^\circ \times 1^\circ$ pixels and TWS
335 from MGB-IPH model was estimated as the weighted mean of TWS of all catchments
336 inside each $4^\circ \times 4^\circ$ pixel, using catchment drainage area as weight. Finally, we
337 computed TWS anomalies using the 2003-2009 long-term average.

338

339 Model performance statistics

340

341 MGB-IPH model results were compared to observations using some statistics
342 commonly used in hydrological modelling studies: (i) Nash-Suttcliffe coefficient ENS ;
343 (ii) log-Nash-Suttcliffe coefficient ENS_{log} (*Collischonn et al.*, 2007), *i.e.* ENS
344 computed using a logarithm transformation on discharge time series to focus on low
345 flows; (iii) relative bias ΔV [%] or BIAS; and (iv) Pearson correlation coefficient R . A
346 “delay index” DI [days] (*Paiva et al.*, 2011b) was used to measure errors related to the

347 time delay between simulated and observed hydrographs. It is computed using the cross
348 correlation function $R_{xy}(m)$ from simulated (x) and observed (y) time series, where DI
349 equals the value of the time lag m where $R_{xy}(m)$ is at maximum. Positive (negative) DI
350 values indicate delayed (advanced) simulated hydrographs. Furthermore, we measured
351 the water level, the TWS and the flood extent amplitude error $A' = 100 \cdot (A_{calc} - A_{obs}) / A_{obs}$,
352 where A_{calc} and A_{obs} are the simulated and observed amplitudes. The amplitude A of a
353 given variable is defined here as the difference between its 95% and 5% percentiles.
354 Due to differences in water levels datum reference and since GRACE actually measures
355 TWS changes, for these variables all model performance statistics (except BIAS) were
356 computed after removing the long-term average.

357

358 **3. Model validation**

359

360 3.1. Discharge

361

362 Validation against river discharges shows a good performance of the MGB-IPH
363 model. According to Fig. 2, in 70% of the stream gauges the $ENS > 0.6$ and model
364 represents mean discharge with accuracy, since volume errors $|\Delta V| < 15\%$ in 75% of the
365 gauges. According to ENS and ΔV values (Fig. 2d), the model performs better in large
366 rivers, although it is sufficiently good in the smaller ones ($ENS > \sim 0.5$ and $|\Delta V| < \sim 20\%$).
367 The flood waves' timing is also well represented by the model and $DI < 5$ days in 70%
368 of the stream gauges. DI values increase in large rivers and, for example, simulated
369 flood wave is 5 to 15 days in advance in the Solimões/Amazon main stem. However,
370 these values can be considered small if compared to the large flood traveling times of
371 Amazon large rivers (a couple of months).

372 Most of the errors are concentrated in rivers draining westerly areas in Bolivia,
373 Peru and Colombia, where the model underestimates discharges. However, these errors
374 can compensate each other and provide feasible discharge results in downstream rivers.
375 We speculate that such errors are a consequence of the poor quality of TRMM 3B42
376 rainfall datasets in these areas, which are poorly monitored and/or mountainous. This is
377 supported by the sensitivity analysis of section 4, which shows that errors in
378 precipitation cause large changes in mean discharge and as well as in water depths and
379 flood extent. Errors in satellite rainfall estimates over the Andean region of the Amazon
380 were also shown by *Condom et al.* (2010) and by *Tian and Peters-Lidard* (2010) in a
381 global map of uncertainties of satellite precipitation estimates.

382 Results for the main Amazon tributaries are promising (Fig. 3). A very good
383 model performance can be found in Juruá and Purus River basins, where the model is
384 able to represent complex (noisy) hydrographs in the upper part and flood waves
385 attenuations as they travel downstream (see Fig. 3c for lower Purus). For the Madeira
386 River basin, errors are found mostly in the Bolivian region (Fig. 2), but in most of
387 Brazilian tributaries and in the Madeira main stem the discharge is well represented
388 (Fig. 3d). Satisfactory model results are also found at Tapajós River basin (Fig. 3e),
389 where hydrographs are mostly dominated by direct runoff and base flow, since large
390 floodplains are not present (see Fig. 7). At Japurá River, which drains parts of the Andes
391 of Colombia and Peru, the model results are poor, as shown in Fig. 3a. At Negro River
392 basin, better results are found mostly in the Branco River basin (northeast) and worst
393 results in the upper Negro River (northwest), but it shows improvement in lower Negro
394 River.

395 Although there are large errors in the upper part of the Solimões river basin in
396 Peru, flood waves are well represented in the Solimões/Amazon main stem, as shown in

397 Fig. 3f and 3g at Tamshiyacu and Manacapuru, respectively. At Óbidos site, located
398 close to the Amazon River outlet, results (Fig. 3h) show a good performance of the
399 MGB-IPH model. *ENS* is high (0.89), the volume error is low (-4.6%) and flood wave is
400 advanced in only -11 days. Hydrological extremes such as the 2005 drought and the
401 2009 flood are well represented (Fig. 3h) and the model captured inter-annual
402 variability (Fig. 4).

403

404 3.2. Water levels

405

406 Validation against water levels from stream gauges shows that the model is
407 performing well in the major tributaries of the Amazon (Fig. 5). *ENS* > 0.60 in 55% of
408 the stream gauges and *R* > 0.8 in 80% of the cases. Water level results are similar to the
409 observations in large rivers, such as in the Solimões River (Fig. 6a) and also in smaller
410 rivers where fast flood waves are present, such as in the Acre River in the upper Purus
411 basin (Fig. 6b). Timing of flood waves are well represented in most gauges (*DI* < 5 days
412 in 80% of the cases). Validation against ENVISAT satellite altimetry data also shows
413 that the model performs well, mostly in central Amazon, Solimões, Juruá (Fig. 6d),
414 Branco (Fig. 6e) and Madeira River and *ENS* > 0.6 in 60% of the virtual stations.

415 However, large errors are found in some sites. A part of them is located in rivers
416 draining poorly monitored and/or mountainous areas where discharges are also poorly
417 simulated (see section 3.1). In some of the stream gauges, despite the fact that the
418 observed and simulated water levels are highly correlated and *DI* values are low, large
419 amplitude errors are present, which indicates that model errors are due to the uncertainty
420 of local cross section geometry, *e.g.* river width. In other sites located mainly close to a
421 confluence with a large river (*e.g.* lower Tapajós River in Fig. 6c), there are large errors

422 of timing and shape of flood waves, probably because either simulated or observed
423 water levels are controlled by both upstream flow and backwater effects. In this case,
424 errors in river bottom level estimates could give rise to errors in the extension of
425 backwater effects and in the timing of flood waves (similar to *Paiva et al.* 2012). We
426 also found a large bias between model and ENVISAT water levels, ranging from -3 to -
427 15 m (Fig. 5). Smaller bias values were found by *Yamazaki et al.* (2012b) in the
428 Amazon main stem, and differences may be associated to different methods for
429 extracting errors from the DEM. In addition, important errors are found in lower
430 Amazon River (Fig. 5 and 6f). The correlation with the observations is very high but the
431 model strongly underestimates the amplitude of water levels. Such errors could be due
432 to errors in river width estimates and also due to DEM, and therefore floodplain
433 geometry errors, which cause errors in flood extent and consequently in river-floodplain
434 volume exchanges, as supported by the sensitivity analysis presented in Section 4.

435

436 3.3. Flood extent

437

438 The overall inundation extent results from the MGB-IPH model are similar to
439 remote sensing estimates from *Papa et al.* (2010) showing the seasonal variation of
440 flood extent and the north-south contrast, with flood peaks occurring in DJF and MAM
441 at the Bolivian Amazon, in MAM and JJA at central Amazon and JJA in the north (Fig.
442 7).

443 The model provides total inundation extent similar to remote sensing estimates
444 (Fig. 8) for the whole Amazon basin, with relatively good model performance statistics:
445 $ENS = 0.71$, $R = 0.92$, $A' = -26\%$ and $BIAS = -7\%$. However, analyses in different

446 regions (rectangles in Fig. 7) show that errors are compensated when generating the
447 overall estimate.

448 The best model results are found in central Amazon (Fig. 8), where a relatively
449 low amplitude error (12%), bias (14%) and high correlation coefficient (0.85) are found.
450 In the Peruvian Amazon (Fig. 8c) the model overestimates flood extent although the
451 seasonal variation is well represented, while in the Bolivian Amazon (Fig. 8b), low
452 water period and seasonal variation are well captured by the model, but flood at high
453 water period is underestimated (DJF and MAM). In lower Amazon (Fig. 8d), bias is
454 only -30 % and the seasonal variation is well represented ($R = 0.90$). However, the
455 model underestimates the amplitude and flood at the high water period, leading to a low
456 *ENS* value. This is in accordance with errors in water levels presented in section 3.2.

457 It is noteworthy that a part of the errors could come from the remote sensing
458 observations. A previous and similar dataset (*Prigent et al., 2007*) seems to
459 overestimate flood extent in the lower Amazon and underestimate it in the Solimões
460 floodplain (central Amazon) if compared to *Hess et al. (2003)* dual season estimates for
461 1996 high water and 1995 low water periods.

462 Errors in flood extent may be due to uncertainty in river-floodplain geometry
463 parameters, as presented in Section 4. For example, important errors are found in water
464 levels and inundation extent in the lower Amazon River. In both cases, model results are
465 highly correlated with observations, but the model underestimated the amplitude of
466 water levels and flooded area. We speculate that the errors in lower Amazon River are
467 due to river width errors and due to DEM errors. We used a coarser version of SRTM
468 DEM with a ~500 m resolution instead of the ~90m, while floodplain flows can be
469 partly controlled by smaller scale topography such as small channels (*Trigg et al.,*
470 2012). Besides, the SRTM DEM has systematic errors related to vegetation and surface

471 water effects (*Sun et al.*, 2003). We corrected these errors using methods presented in
472 *Paiva et al.* (2011a) for river bottom level estimation and subtracting a constant value of
473 $H_{veg}=17$ m in all DEM pixels, except where there is low vegetation. However,
474 vegetation height may be variable even in forested areas. For example, in lower
475 Amazon, large marginal lakes are present in floodplain (*e.g. Melack and Hess*, 2010;
476 *Bonnet et al.*, 2008) and due to the correction applied in DEM, they are always flooded
477 in the model simulation. Furthermore, a small water level variation leads to less river-
478 floodplain volume exchanges.

479

480 3.4. Terrestrial water storage

481

482 Analyses show that the model provides TWS in good accordance with GRACE
483 estimates. *ENS* values for TWS over the whole Amazon is 0.93, the correlation
484 coefficient is high (0.97) and the amplitude error is low (12%). Fig. 9d shows that
485 interannual variability is represented by the model, including the 2005 drought and the
486 2009 flood.

487 We also examined results in 21 square sub-regions with spatial resolution of $4^\circ \times$
488 4° . *ENS* < 0.8 and *R* < 0.9 only in 5 areas, and these are found mostly in the northwest
489 part of the Amazon and in upper Branco River basin, possibly due to the same errors
490 reported in discharge results related to the precipitation forcing. Also, these areas are
491 concentrated in the border of the river basin, where the Gaussian filter applied to the
492 model results may have added errors. In other parts of the Amazon, results were
493 provided in accordance with GRACE estimates (*e.g.* Fig. 9b,c). Amplitude errors are
494 larger than 20% only in 5 sub-regions, located in west, but also in lower Amazon River.

495 In the latter, errors are in accordance with the underestimation of water level and flood
496 extent amplitude presented in sections 3.2 and 3.3.

497

498 **4. Sensitivity analysis**

499

500 We performed a sensitivity analysis to investigate the sources of model errors
501 and also the physical functioning of the Amazon River basin. The model sensitivity to
502 six model parameters/variables was evaluated: river width, manning's roughness
503 coefficient, river bottom level, precipitation, flooded area and maximum soil storage. In
504 all cases, each parameter/variable was equally perturbed in all Amazon river basin by
505 the factors +50, +20, 0, -20 and -50%, except for river bottom level where we used
506 +3,+1,0,-1,-3 m. Results were evaluated in terms of discharge close to the basin outlet at
507 Óbidos station (Obd site at Fig. 1), water depth at central Amazon at Manacapuru
508 station (Man site at Fig. 1) and total flooded area (Fig. 10 and 11) using climatological
509 values computed from the 1999 to 2009 time period.

510 An important interaction between water levels, flooded areas and discharge
511 occurs during flood waves traveling (Fig. 10). A decrease in river width causes a large
512 increase in water depths and levels, consequently an increase of flooded areas occurs
513 and flood waves are attenuated and delayed in a couple of months, causing minor flood
514 flows and droughts, although the mean discharge does not change. Still, an increase in
515 river width decreases water depth and flood inundation, resulting in advanced flood
516 waves and major high water discharges. An explanation would be that larger amounts of
517 water are stored and released across the floodplains, causing larger flow travel times.
518 An inverse effect is observed perturbing manning's roughness coefficient. River width

519 and manning coefficient results are similar to those discussed by *Yamazaki et al.* (2011)
520 about river and floodplain interactions and flood wave travel times.

521 Increasing river bottom levels causes, at first, a smaller difference between river
522 and floodplain bottom levels and as a result, flooding is easier to occur. Consequently,
523 flood extension increases and the aforementioned effect takes place with a delayed flood
524 wave. However, now water depth decreases possibly because larger amounts of water
525 enter in floodplains.

526 Precipitation is the most sensitive variable (Fig. 10) and increasing it
527 dramatically increases mean discharge, water depths and flood extent. Also, the same
528 river-floodplain interaction takes place and flood waves are delayed and attenuated,
529 although changes in mean values are much more pronounced.

530 Positive changes in flooded areas (from the z vs Afl curve derived from the
531 SRTM DEM) cause a similar effect than that observed in the river bottom level, with a
532 decrease in water depths and delayed and attenuated flood waves (Fig. 11). Finally, we
533 examined maximum soil water storage (Fig. 11), the most sensitive parameter of
534 vertical water/energy balance of the MGB-IPH model (*Collischonn, 2001*). Positive
535 perturbations decrease all variables, probably because larger amounts of available water
536 in the soil facilitate larger evapotranspiration rates. However, the sensibility of this
537 parameter is not as pronounced as the others.

538 It is worth mentioning that we evaluated errors equally distributed over the
539 entire basin, and that local uncertainties can cause different kinds of errors in
540 discharges, water depths and flood extent. For example, errors in river width in a small
541 reach may cause errors in both the mean and amplitude of water depths, and
542 consequently in local flood extent, but may not have a major influence over other parts
543 of the basin.

544 The analysis shows that input data uncertainty might play an important role in
545 model errors. The model results are very sensitive to river – floodplain parameters,
546 indicating the need to improve current estimation methods, which are based mostly in
547 geomorphological relations and information from the SRTM DEM. These conclusions
548 are consistent with recommendations from other modelling studies using global river-
549 flood models (*Decharme et al., 2011; Yamazaki et al., 2011*) and a flood inundation
550 model (*Wilson et al., 2007*). Data from field campaigns could be used, but also methods
551 using remote sensing to estimate river width and bottom level should be investigated,
552 such as in *Durand et al. (2010a)*. Also, either a new DEM or a more sophisticated
553 correction of the SRTM DEM is needed, removing vegetation height in forested areas
554 and estimating bottom level of floodplain lakes. Vegetation effects could be removed,
555 for example, using a global vegetation height map, such as in *Simard et al. (2011)*.
556 Water level effects could be removed using a combination of satellite altimetry water
557 levels and flood extent data, such as the techniques used by *Frappart et al. (2008;*
558 *2011a)* to estimate floodplain volumes variation. DEM corrections to allow better flow
559 connectivity in small channels connecting floodplains such as presented by *Yamazaki et*
560 *al. (2012)* could also be used. Additionally, data from the future Surface Water and
561 Ocean Topography (SWOT) mission could also be employed (*Durand et al., 2010b*).

562

563

564

565

566 **5. Aspects of Amazon hydrological processes**

567

568

569 5.1 Water balance

570

571 Fig. 12 presents the main components of water balance of the Amazon basin,
572 comprising mean precipitation (P), evapotranspiration (ET) and discharge (Q) at Óbidos
573 station rates derived from model results. Mean annual rates for the 1998-2009 period are
574 $P = 5.65$ mm/day, $ET = 2.72$ mm/day and $Q = 3.09$ mm/day. As discussed in section
575 3.1., simulated discharge is similar to observations at Óbidos station, with a small bias
576 equal to -4.6%. Mean precipitation, which is based on TRMM 3B42 v6 data, is slightly
577 smaller (~6%) than values obtained in others: 6.0 mm/day from *Espinoza et al.* (2009)
578 based on 756 pluviometric stations; 6.3 mm/day from *Azarderakhsh et al.* (2011) based
579 on GPCP remote sensing data; 5.8 (5.2 – 8.6) mm/day by *Marengo et al.* (2005) based
580 on several rain gauges, remote sensing and reanalyses-based data. ET rates are also
581 comparable with values obtained in other studies, although there are large differences
582 between them: 2.27 mm/day by *Azarderakhsh et al.* (2011) using global remote sensing-
583 based products; 4.3 mm/day by *Marengo et al.* (2005); 3.23 mm/day by *Ruhoff* (2011)
584 using MOD16 remote sensing product but including the Tocantins basin; 3.2 mm/day
585 (at Negro basin), 2.9-3.8 mm/day and 2.6-3.0 mm/day using modeling results by
586 *Getirana et al.* (2010), *Costa and Foley* (1997) and *Beighley et al.*, (2009),
587 respectively.

588 P exhibits a large seasonal variation, with larger rates ($P > 7$ mm/day) between
589 December and April with the maximum at February and March ($P \sim 8.5$ mm/day) and
590 minimum values at July and August ($P \sim 2.5$ mm/day). The mean Amazon ET is almost
591 constant along the year, without significant seasonal variations. The combination of P
592 and ET rates causes a marked seasonal behaviour in discharge, with maximum
593 (minimum) values of 4.3 (1.9) mm/day, occurring in May-June (October-November).

594 Discharge signal is delayed in 3 months if compared with P , showing the large water
595 travel times along the Amazon rivers and floodplains.

596 Although the seasonally inundated floodplains play an important role in water
597 transport throughout the Amazonian rivers, as demonstrated by the sensitivity analysis
598 and by the results shown in next section, it seems not to have a major influence in water
599 balance. Fig. 12 show a comparison of Q and ET results from two simulations, one
600 considering the effect of seasonal flooded areas on ET (using methods described in
601 *Paiva et al.* 2011a) and the other without such consideration, and the differences
602 between them are insignificant. Although this is a preliminary analysis, and since ET
603 from flooded forests is not completely represented using the Penman Monteith
604 approach, a possible explanation could be that (i) flooded areas represent a small part
605 (less than 5%) of the total area of the Amazon and that (ii) ET in the Amazon is driven
606 mostly by radiation (*Costa et al.*, 2010) and not by water availability and consequently
607 ET rates from flooded and nonflooded forests are similar.

608

609 5.2 Terrestrial water storage

610

611 In this section, the Amazon terrestrial water storage changes and the role of
612 surface, soil and ground waters on TWS are explored. Analyses of Fig. 9 based on
613 GRACE data show a marked seasonal variability of terrestrial water storage with large
614 amplitude of variation (325 mm, mean of all GRACE solutions). Larger TWS variations
615 are found mostly in central Amazon, with amplitudes of TWS larger than 750 mm, and
616 smaller values are found in the Andean region (< 300 mm). To evaluate the main
617 contributors of the TWS variations, we computed the water storage of three major
618 hydrological compartments using model results, namely surface water (sum of river,

619 floodplain and surface runoff storages), soil water and ground water and calculated the
620 respective amplitude of variation as described in Section 2. The amplitude of variation
621 of surface waters governs most of TWS changes in the Amazon basin (see Fig. 13),
622 mostly in central Amazon and areas with large floodplains (see Fig. 7 and 13a). Soil
623 water presents an important contribution on TWS changes in south-eastern areas; whilst
624 ground water is the least important compartment in almost all regions. Surface waters
625 dominate TWS variations for the whole Amazon area with a fraction of 56%, followed
626 by soil (27%) and ground water storages (8%) (see Fig. 13b). Also, surface and soil
627 water present similar seasonal variation, while groundwater storage presents a small
628 delay. Results agree with *Han et al.* (2009) and *Frappart et al.* (2008), which indicated
629 the dominant role of surface waters in TWS variations in the Amazon. The results also
630 agree with *Frappart et al.* (2011a) that, using mostly remotely sensed datasets at the
631 Negro river basin, showed that TWS changes are dominated by surface waters followed
632 by soil and ground water with similar importance. Our results are also similar with *Kim*
633 *et al.* (2009) estimates for the Amazon in a global study using modelling results, where
634 river storage including shallow ground water (soil moisture) explained 73% (27%) of
635 total TWS changes.

636

637 5.3 River - floodplain hydraulics

638

639 To finish our analyses of the Amazon hydrological processes, river and
640 floodplain processes are investigated and the importance of backwater effects and flood
641 inundation in stream flow routing is evaluated. We compared discharge results from
642 four model runs using the same parameters and model input forcings in all of them, but
643 with different kinds of stream flow routing methods: (i) HDf - hydrodynamic model

644 with floodplains, equal to model configuration used in the rest of the manuscript; (ii)
645 MCf – Muskingum Cunge Todini with floodplains, using a nonlinear version of the
646 Muskingum Cunge as presented by *Todini* (2007) and extended by *Pontes* (2011) to
647 consider floodplains; (iii) HDn – hydrodynamic model without floodplains; (iv) MCn -
648 Muskingum Cunge without floodplains. The Muskingum Cunge based models, MCf
649 and MCn, do not deal with backwater effects, since they are based on a kinematic wave
650 approximation of the Saint Venant equations and do not consider neither the inertia nor
651 the pressure forces, while HDn and MCn models do not represent flood inundation.

652 Results shown in Fig. 14 and in Table 2 indicate the better performance of the
653 complete hydrodynamic model (HDf) in comparison with the other methods. Including
654 backwater effects and floodplain storage generally delay and attenuates hydrographs,
655 and simulations agree with observations (for example, $ENS = 0.89$ and 0.77 and $DI = -$
656 11 and -10 days at Óbidos and Manacapuru stations respectively). Neither considering
657 backwater effects nor floodplains (MC run) causes very advanced ($DI = -64$ and -76
658 days) and noisy hydrographs, with low ENS values ($ENS = -0.51$ and -1.44) and
659 discarding only flood inundation (HDn run) causes a similar effect. However, to include
660 floodplains only (MCf) is not sufficient to reproduce observed discharges ($ENS = 0.72$
661 and 0.31) and hydrographs still advanced about 15 and 25 days if compared to the most
662 complete model (HDf). Possibly, the influence of floodplains is increased when the
663 pressure term is present, as discussed in *Paiva et al.* (2012).

664 These results suggest that floodplains play a major role in flood wave
665 attenuation and delay, but that backwater effects also cause important impacts. They are
666 in accordance with preliminary analyses from *Paiva et al.* (2012), but they disagree with
667 *Yamazaki et al.* (2011), who presented similar conclusions about floodplain storage but

668 stated that backwater effects have a minor impact on hydrographs and are more
669 important for representing water level profiles.

670 Although discussions from previous sections indicate that the model errors may
671 arise from uncertainty in input data, results from this section show the importance of the
672 model structure. Our approach is relatively complex in terms of river hydraulics since it
673 uses full *Saint-Venant* equations, but is somehow simplified in terms of floodplain
674 simulation. Consequently, it cannot fully represent all aspects of floodplain
675 hydrodynamics such as bidirectional flows and river-floodplain water level dynamics
676 (*Alsdorf et al. 2007a; Alsdorf et al., 2003; Bonnet et al., 2008*) and flow in small
677 floodplain channels (*Trigg et al., 2012*). We believe that different flood inundation
678 approaches (*e.g. Bonnet et al., 2008; Paz et al., 2011; Wilson et al., 2007; Bates and De*
679 *Roo, 2000; Neal et al. 2012*) coupled with full hydrodynamic models should still be
680 tested to check its feasibility to represent all floodplain processes and the influence of
681 these processes in large-scale stream flow routing and inundation dynamics.

682

683 **6. Summary and conclusions**

684

685 We present an extensive validation of the physically based large-scale
686 hydrologic and hydrodynamic model MGB-IPH in the Amazon River basin using *in situ*
687 and remote sensing data sets. Sources of model errors, which can be extrapolated to
688 other similar large scale models, were investigated by using model validation results
689 and also supported by sensitivity tests. Finally, aspects of the physical functioning of the
690 Amazon River basin are discussed taking advantage of the model results.

691 The model is able to reproduce observed hydrographs at different spatial scales,
692 although performance is usually better in large rivers with large flood wave travel times.

693 The model provides feasible water level results in most of the gauging stations and also
694 at altimetry-based validation sites and overall inundation extent results similar to the
695 remote sensing estimates. Discharge is well simulated even in regions where other
696 hydrological variables are not well represented, as in the lower Amazon where some
697 errors in water levels and flood extent can be found. Terrestrial water storage results
698 also agree with GRACE-derived estimates.

699 Results from the sensitivity analysis indicate that model input data uncertainty
700 may play an important role in model errors such as the ones presented in the model
701 validation, although part of them can be due to the uncertainty in remote sensing data
702 used here as observations. Precipitation forcing is the most sensitive variable, causing
703 significant errors in mean discharge, water depth and flood extent. At the same time,
704 important errors occur in westerly areas, which may be a consequence of the poor
705 quality of TRMM 3B42 rainfall datasets in these areas, which are mountainous and/or
706 poorly monitored.

707 The model results are also very sensitive to river-floodplain parameters,
708 including river width and bottom level, Manning roughness coefficient and floodplain
709 bathymetry. Important interactions between water levels, flooded areas and discharge
710 errors are observed during the floodwaves traveling. Uncertainty in river and floodplain
711 geometry, estimated through geomorphological relations and the SRTM DEM, causes
712 errors in simulated water levels and inundation extent in some areas, indicating the need
713 for improving current parameter estimation methods. These parameters are similar to
714 the ones required in other large scale models and its uncertainty may cause errors in
715 these models as well. Some alternatives to that could be the usage of newly remote
716 sensing techniques for parameter estimation or corrections of the SRTM DEM to
717 remove vegetation height in forested areas and to estimate bottom level of floodplains.

718 Overall water balance derived from model results is similar to estimates from
719 previous studies. Mean annual rates of precipitation, evapotranspiration and discharge at
720 Óbidos station are $P = 5.65$ mm/day, $ET = 2.72$ mm/day and $Q = 3.09$ mm/day. TWS
721 changes show marked seasonal variability with a large amplitude of variation of 325
722 mm for all Amazon, and larger amplitude values (>750 mm) are found in central
723 Amazon. Surface waters governs most of TWS changes in the Amazon basin (56%),
724 mostly in central Amazon and in areas with large floodplains, while soil water presents
725 an important contribution to TWS changes (27%), mainly in south-eastern areas and
726 groundwater, it is the less important hydrological compartment (8%).

727 Finally, river and floodplain processes and the importance of backwater effects
728 and flood inundation in stream flow routing were investigated. Results suggest that
729 floodplains play a major role in flood wave attenuation and delay, but that backwater
730 effects also cause important impacts, indicating the importance of including a flood
731 inundation module and a complex *Saint Venant* equation approximation for river
732 floodplain processes modelling in the Amazon. In contrast, although the seasonally
733 inundated floodplains play an important role in water transport along Amazonian rivers,
734 it seems not to have a major influence on evapotranspiration and water balance.

735

736 **Acknowledgements**

737

738 The authors are grateful for: the financial and operational support from the
739 Brazilian agencies FINEP and ANA (“Projeto de Integração e Cooperação Amazônica
740 para a Modernização do Monitoramento Hidrológico” (ICA-MMH)) and CNPq
741 (“Assimilação de Dados de monitoramento Espacial para a análise do regime
742 hidrológico da Bacia Amazônica e a previsão de curto e médio prazos”) and the

743 MHYZPA project funded by the French INSU EC2CO Cytrix program; the global
744 inundation extent dataset provided by Fabrice Papa; the ENVISAT satellite altimetry
745 data provided by Joecila Santos da Silva; the TRMM data supplied by NASA and
746 associated agencies; the discharge data provided by ANA, Hybam, SENHAMI-Peru and
747 SENHAMI-Bolivia; as well for the constructive comments from Dr. Praveen Kumar,
748 editor of WRR, Dr. Augusto Getirana and other two anonymous Reviewers.

749

750 **References**

751

752 Alsdorf, D., Dunne, T., Melack, J., Smith, L., Hess, L. 2003. Diffusion modeling of
753 recessional flow on central Amazonian floodplains. *Geophysical Research Letters*,
754 32, L21405.

755 Alsdorf, D., P. Bates, J. Melack, M. Wilson and T. Dunne, 2007a. The spatial and
756 temporal complexity of the Amazon flood measured from space, *Geophysical*
757 *Research Ltrs.* 34, L08402.

758 Alsdorf DE, Rodriguez E, Lettenmaier DP. 2007b. Measuring surface water from space.
759 *Reviews of Geophysics* 45: RG2002, DOI:10.1029/2006RG000197.

760 Alsdorf, D., Han, S-C., Bates, P., Melack, J. 2010. Seasonal water storage on the
761 Amazon floodplain measured from satellites. *Remote Sensing of Environment*,
762 114, 2448–2456.

763 Azarderakhsh, M., W. B. Rossow, F. Papa, H. Norouzi, and R. Khanbilvardi (2011),
764 Diagnosing water variations within the Amazon basin using satellite data, *J.*
765 *Geophys. Res.*, 116, D24107, doi:10.1029/2011JD015997.

766 Bates, P.D., De Roo, A.P.J., 2000. A simple raster based model for flood inundation
767 simulation. *J. Hydrol.* 236, 54–77.

768 Beighley, R.E., Eggert, K.G., Dunne, T., He, Y., Gummadi, V., Verdin, K.L. 2009.
769 Simulating hydrologic and hydraulic processes throughout the Amazon River
770 Basin. *Hydrological Processes* 23 (8), pp. 1221-1235

771 Biancamaria, S., Bates, P. D., Boone, A., Mognard, N. M. 2009. Large-scale coupled
772 hydrologic and hydraulic modelling of the Ob river in Siberia. *Journal of*
773 *Hydrology* 379. 136–150.

774 Bonnet, M.P; Barroux, G.; Martinez, J.M.; Seyler, F.; Turcq, P.M.; Cochonneau, G.;
775 Melack, J.M.; Boaventura, G.; Bourgoïn, L.M.; León, J.G.; Roux, E.; Calmant, S.;
776 Kosuth, P.; Guyot, J.L.; Seyler, F. 2008. Floodplain hydrology in an Amazon
777 floodplain lake (Lago Grande de Curuaí). *Journal of Hydrology*, 349, 18 - 30 pp.

778 Bourgoïn, L.M., Bonnet, M.P., Martinez, J.M., Kosuth, P., Cochonneau, G., Turcq,
779 P.M., Guyot, J.L., Vauchel, P., Filizola, N., Seyler, P. 2007. Temporal dynamics
780 of water and sediment exchanges between the Curuaí floodplain and the Amazon
781 River, Brazil. *Journal of Hydrology* 335. 140 - 156.

782 Castellarin, A., A., G. Di Baldassarre, P. D. Bates and A. Brath. 2009. Optimal Cross-
783 Sectional Spacing in Preissmann Scheme 1D Hydrodynamic Models. *Journal of*
784 *Hydraulic Engineering*, 135(2), 96-105

785 Chen, J. L., C. R. Wilson, and B. D. Tapley (2010), The 2009 exceptional Amazon
786 flood and interannual terrestrial water storage change observed by GRACE, *Water*
787 *Resour. Res.*, 46, W12526, doi:10.1029/2010WR009383.

788 Coe, M.T., Costa, M.H., Howard, E.A. 2008. Simulating the surface waters of the
789 Amazon River basin: Impacts of new river geomorphic and flow
790 parameterizations. *Hydrological Processes* 22 (14), pp. 2542-2553.

791 Collischonn, W. (2001) Hydrologic simulation of large basins (in Portuguese), PhD
792 Thesis, Inst. de Pesqui. Hidraul., Univ. Fed. do Rio Grande do Sul, Porto Alegre,
793 Brazil.

794 Collischonn, W.; Allasia, D.G.; Silva, B.C.; Tucci, C.E.M. 2007. The MGB-IPH model
795 for large-scale rainfall-runoff modeling. *Hydrological Sciences Journal*, 52, 878-
796 895 pp.

797 Collischonn, B.; Collischonn, W.; Tucci, C. 2008 Daily hydrological modeling in the
798 Amazon basin using TRMM rainfall estimates. *Journal of Hydrology*, p. 207.

799 Condom, T., Rau, P.; Espinoza, J. C. (2010) Correction of TRMM 3B43 monthly
800 precipitation data over the mountainous areas of Peru during the period 1998–
801 2007. *Hydrol. Processes* DOI: 10.1002/hyp.7949.

802 Costa MH, Foley JA. 1997. Water balance of the Amazon Basin: dependence on
803 vegetation cover and canopy conductance. *Journal of Geophysical Research-*
804 *Atmospheres* 102(D20): 23973–23989.

805 Costa, M. H., M. C. Biajoli, L. Sanches, A. C. M. Malhado, L. R. Hutyra, H. R. da Rocha,
806 R. G. Aguiar, and A. C. de Araújo (2010), Atmospheric versus vegetation controls
807 of Amazonian tropical rain forest evapotranspiration: Are the wet and seasonally
808 dry rain forests any different?, *J. Geophys. Res.*, 115, G04021,
809 doi:10.1029/2009JG001179.

810 Cunge, J.A.; Holly, F.M.; Verney, A. 1980. *Practical Aspects of Computational River*
811 *Hydraulics*. Pitman Advanced Publishing Program.

812 Decharme, B.; R. Alkama, F. Papa, S. Faroux, H. Douville, C. Prigent. (2011) Global
813 off-line evaluation of the ISBA-TRIP flood model. *Climate Dynamics*.

814 Dijkshoorn, J.A.; Huting, J.R.M.; Tempel, P. 2005. Update of the 1:5 million Soil and
815 Terrain Database for Latin America and the Caribbean (SOTERLAC; version
816 2.0). Report 2005/01, ISRIC – World Soil Information, Wageningen.

817 Durand, M., Rodríguez, E., Alsdorf, D., Trigg, M. 2010a. Estimating River Depth From
818 Remote Sensing Swath Interferometry Measurements of River. IEEE journal of
819 selected topics in applied earth observations and remote sensing. 3. 20-31.

820 Durand, M., Fu, L. L., Lettenmaier, D. P., Alsdorf, D. E., Rodríguez, E., & Fernandez,
821 D. E. (2010b). The surface water and ocean topography mission: Observing
822 terrestrial surface water and oceanic submesoscale eddies. Proceedings Of the
823 IEEE, 98(5), 766–779.

824 Espinoza JC., J. Ronchail, J.L. Guyot, Cocheneau G., N Filizola, W. Lavado, E. de
825 Oliveira, R. Pombosa and P. Vauchel: Spatio – Temporal rainfall variability in the
826 Amazon Basin Countries (Brazil, Peru, Bolivia, Colombia and Ecuador).
827 International Journal of Climatology, 29, 1574-1594, 2009.

828 Espinoza, J. C., J. Ronchail, J. L. Guyot, C. Junquas, P. Vauchel, W. Lavado, G.
829 Drapeau, and R. Pombosa (2011), Climate variability and extreme drought in the
830 upper Solimões River (western Amazon Basin): Understanding the exceptional
831 2010 drought, Geophys. Res. Lett., 38, L13406, doi:10.1029/2011GL047862.

832 Eva, H.D.; De Miranda, E.E.; Di Bella, C.M.; Gond, V. 2002. A Vegetation map of
833 South America. EUR 20159 EN, European Commission, Luxembourg.

834 Farr, T.G., Caro, E., Crippen, R., Duren, R., Hensley, S., Kobrick, M., Paller,
835 M.,Rodriguez, E., Rosen, P., Roth, L., Seal, D., Shaffer, S., Shimada, J., Umland,
836 J.,Werner, M., Burbank, D., Oskin, M., and Alsdorf, D. 2007. The shuttle
837 radartopography mission, Reviews of Geophysics, 45(2).

838 Frappart F., Papa F., Famiglietti J.S., Prigent C., Rossow W.B., Seyler F.
839 (2008). Interannual variations of river water storage from a multiple satellite
840 approach: a case study for the Rio Negro River basin, *Journal of Geophysical*
841 *Research*, 113(D21), D21104, doi:10.1029/2007JD009438.

842 Frappart, F.; Papa, F.; Guntner, A.; Werth, S.; Santos da Silva, J.; Tomasella, J.; Seyler,
843 F.; Prigent, C.; Rossow, W.B.; Calmant, S.; Bonnet, M.P. 2011a. Satellite-based
844 estimates of groundwater storage variations in large drainage basins with
845 extensive floodplains. *Remote Sensing of Environment*. 115, 6, 1588-1594.

846 Frappart F., Ramillien G., Maisongrande P., Bonnet M-P. (2010). Denoising satellite
847 gravity signals by Independent Component Analysis, *IEEE Geosciences and*
848 *Remote Sensing Letters*, 7(3), 421-425, doi:10.1109/LGRS.2009.2037837.

849 Frappart F., Ramillien G., Leblanc M., Tweed S.O., Bonnet M-P., Maisongrande P.
850 (2011b). An Independent Component Analysis approach for filtering continental
851 hydrology in the GRACE gravity data, *Remote Sensing of Environment*, 115(1),
852 187-204, doi: 10.1016/j.rse.2010.08.017.

853 Getirana, A. C. V.; Bonnet, M.-P.; Rotunno Filho, O. C.; Collischonn, W.; Guyot, J.-L.;
854 Seyler, F.; Mansur, W. J. 2010 Hydrological modelling and water balance of the
855 Negro River basin: evaluation based on in situ and spatial altimetry data.
856 *Hydrological Processes* 24 (22), pp. 3219-3236.

857 Getirana et al. 2011. Calibração e Validação de Modelo Hidrológico com Observações
858 In Situ, Altimetria e Gravimetria Espaciais. *RBRH — Revista Brasileira de*
859 *Recursos Hídricos* Volume 16 n.1 Jan/Mar 2011, 29-45.

860 Getirana, A. C. V., Boone, A., Yamazaki, D., Decharme, B., Papa, F., and Mognard, N.:
861 The Hydrological Modeling and Analysis Platform (HyMAP): evaluation in the
862 Amazon basin, *J. Hydrometeorol.*, accepted for publication, 2012.

863 Han, S.-C., H. Kim, I.-Y. Yeo, P. Yeh, T. Oki, K.-W. Seo, D. Alsdorf, and S. B.
864 Luthcke (2009), Dynamics of surface water storage in the Amazon inferred from
865 measurements of inter-satellite distance change, *Geophys. Res. Lett.*, 36, L09403,
866 doi:10.1029/2009GL037910.

867 Hess, L.L.; Melack, J.M.; Novo, E.M.L.M.; Barbosa, C.C.F.; Gastil, M. 2003. Dual-
868 season mapping of wetland inundation and vegetation for the central Amazon
869 basin. *Remote Sensing of Environment*, 87, 404 – 428 pp.

870 Huffman, G., Adler, R., Bolvin, D., Gu, G., Nelkin, E., Bowman, K., Hong, Y., Stocker,
871 E.; Wolff, D. (2007) The TRMM Multisatellite Precipitation Analysis (TCMA):
872 quasi-global, multiyear, combined-sensor precipitation estimates at fine scales. *J.*
873 *Hydromet.* 8, 38–55.

874 Junk, W.J., 1997. General aspects of floodplain ecology with special reference to
875 Amazonian floodplains. In: Junk, W.J. (Ed.), *The Central-Amazonian Floodplain:*
876 *Ecology of a Pulsing System*, Ecological Studies. Springer Verlag/Heidelberg,
877 Berlin/New York, pp. 3–22.

878 Kim, H., P. J.-F. Yeh, T. Oki, and S. Kanae (2009), Role of rivers in the seasonal
879 variations of terrestrial water storage over global basins, *Geophys. Res. Lett.*, 36,
880 L17402, doi:10.1029/2009GL039006.

881 Kosuth, P., Callède, J., Laraque, A., Filizola, N., Guyot, J.L., Seyler, P., Fritsch, J.M.,
882 Guimarães, V. 2009 Sea-tide effects on flows in the lower reaches of the Amazon
883 River. *Hydrological Processes* 23 (22), pp. 3141-3150.

884 Lian, Y.; Chan, I.-C.; Singh, J.; Demissie, M.; Knapp, V.; Xie, H. 2007 Coupling of
885 hydrologic and hydraulic models for the Illinois River Basin. *Journal of*
886 *Hydrology* 344, 210– 222.

887 Marengo JA. 2005. Characteristics and spatio-temporal variability of the Amazon River
888 basin water budget. *Climate Dynamics* 24: 11–22. DOI 10.1007/s00382-004-
889 0461-6.

890 Marengo, J., Nobre, C., Tomasella, J., Oyama, M., de Oliveira, G., de Oliveira, R.,
891 Camargo, H., Alves, L. 2008. The drought in Amazonia in 2005. *Journal of*
892 *Climate*, 21:495–516.

893 Marengo, J. A., J. Tomasella, L. M. Alves, W. R. Soares, and D. A. Rodriguez (2011),
894 The drought of 2010 in the context of historical droughts in the Amazon region,
895 *Geophys. Res. Lett.*, 38, L12703, doi:10.1029/2011GL047436

896 Meade, R.H., Rayol, J.M., Da Conceição, S.C., Natividade, J.R.G. 1991. Backwater
897 effects in the Amazon River basin of Brazil . *Environmental Geology and Water*
898 *Sciences* 18 (2), 105-114 pp.

899 Melack, J.M., Hess, L.L., Gastil, M., Forsberg, B.R., Hamilton, S.K., Lima, I.B.T.,
900 Novo, E.M.L.M., 2004. Regionalization of methane emissions in the Amazon
901 basin with microwave remote sensing. *Global Change Biol.* 10, 530–544.

902 Melack JM, Hess LL (2010) Remote sensing of the distribution and extent of wetlands
903 in the Amazon basin. In Junk WJ, Piedade M (eds) *Amazonian floodplain forests:*
904 *ecophysiology, ecology, biodiversity and sustainable management.* *Ecological*
905 *Studies*, vol. 210, part 1. Springer, pp 43–59.

906 Mohamed, Y. A., van den Hurk , B. J. J. M., Savenije, H. H. G., Bastiaanssen, W. G. M.
907 2005. Impact of the Sudd wetland on the Nile hydroclimatology, *Water Resour.*
908 *Res.*, 41, W08420.

909 New, M., Lister, D., Hulme, M. & Makin, I. (2002) A high-resolution data set of surface
910 climate over global land areas. *Climate Res.* 21.

911 Neal, J. C., G. J.-P. Schumann, and P. D. D. Bates (2012), A sub-grid channel model for
912 simulating river hydraulics and floodplain inundation over large and data sparse
913 areas, *Water Resour. Res.*, doi:10.1029/2012WR012514, in press.

914 Paiva, R.C.D.; Collischonn, W.; Tucci, C.E.M. 2011a. Large scale hydrologic and
915 hydrodynamic modeling using limited data and a GIS based approach. *Journal of*
916 *Hydrology*. 406, 170–181

917 Paiva, R. C. D., D. C. Buarque, R. T. Clarke, W. Collischonn, and D. G. Allasia. 2011b.
918 Reduced precipitation over large water bodies in the Brazilian Amazon shown
919 from TRMM data, *Geophys. Res. Lett.*, 38, L04406, doi:10.1029/2010GL045277.

920 Paiva, R.C.D., Collischonn, W., Buarque, D.C. 2012. Validation of a full hydrodynamic
921 model for large scale hydrologic modelling in the Amazon. *Hydrol. Process.* DOI:
922 10.1002/hyp.8425

923 Papa, F., C. Prigent, F. Aires, C. Jimenez, W. B. Rossow, and E. Matthews (2010),
924 Interannual variability of surface water extent at the global scale, 1993–2004, *J.*
925 *Geophys. Res.*, 115, D12111, doi:10.1029/2009JD012674.

926 Paz, A. R., Bravo, J. M., Allasia, D., Collischonn, W., Tucci, C. E. M. 2010 Large-Scale
927 Hydrodynamic Modeling of a Complex River Network and Floodplains. *Journal*
928 *of Hydrologic Engineering* 15(2), 152–165.

929 Paz, A. R. d., Collischonn, W., Tucci, C. E. M. and Padovani, C. R. (2011), Large-scale
930 modelling of channel flow and floodplain inundation dynamics and its application
931 to the Pantanal (Brazil). *Hydrological Processes*, 25: 1498–1516. doi:
932 10.1002/hyp.7926

933 Ponce, V.M. 1989. *Engineering Hydrology*. Prentice Hall.

934 Pontes, P.R.M. (2011) Comparing simplified hydrodynamic models for flow routing in
935 rivers and channels (in Portuguese), PhD Thesis, Inst. de Pesqui. Hidraul., Univ.

936 Fed. do Rio Grande do Sul, Porto Alegre, Brazil.
937 <http://hdl.handle.net/10183/35350>

938 Prigent, C., F. Papa, F. Aires, W. B. Rossow, and E. Matthews (2007), Global
939 inundation dynamics inferred from multiple satellite observations, 1993–2000, J.
940 Geophys. Res., 112, D12107, doi:10.1029/2006JD007847.

941 Prigent, C., N. Rochetin, F. Aires, E. Defer, J.-Y. Grandpeix, C. Jimenez, and F. Papa
942 (2011), Impact of the inundation occurrence on the deep convection at continental
943 scale from satellite observations and modeling experiments, J. Geophys. Res.,
944 116, D24118, doi:10.1029/2011JD016311.

945 RADAMBRASIL. 1982. Programa de Integração Nacional, Levantamento de Recursos
946 Naturais. Ministério das Minas e Energia, Secretaria-Geral.

947 Ramillien, G., Famiglietti, J. S., & Wahr, J. (2008). Detection of continental hydrology
948 and glaciology signals from GRACE: A review. *Surveys in Geophysics*, 29(4–5),
949 361–374. doi:10.1007/s10712-008-9048-9

950 Ramillien, G., Frappart, F., Cazenave, A., & Güntner, A. (2005). Time variations of the
951 land water storage from an inversion of 2 years of GRACE geoids. *Earth and
952 Planetary Science Letters*, 235, 283–301. doi:10.1016/j.epsl.2005.04.005

953 Renno, C.D.; Nobre, A.D.; Cuartas, L.A.; Soares, J.V.; Hodnett, M.G.; Tomasella, J.;
954 Waterloo, M.J. 2009. HAND, a new terrain descriptor using SRTM-DEM:
955 Mapping terra-firme rainforest environments in Amazonia. *Remote Sensing of
956 Environment*, 12, 9, 3469-3481.

957 Richey, J. E., Melack, J. M., Aufdenkampe, A. K., Ballester, V.M., & Hess, L. L. 2002.
958 Outgassing from Amazonian rivers and wetlands as a large tropical source of
959 atmospheric CO₂. *Nature* 416, 617–620.

960 Ruhoff, A.L. (2011) Remote sensing applied to evapotranspiration estimation in tropical
961 biomes (in Portuguese), PhD Thesis, Inst. de Pesqui. Hidraul., Univ. Fed. do Rio
962 Grande do Sul, Porto Alegre, Brazil. <http://hdl.handle.net/10183/32468>

963 Santos da Silva, J.; Calmant, S.; Seyler, F.; Rotunno Filho, O.C.; Cochonneau, G.;
964 Mansur, W.J. 2010. Water levels in the Amazon basin derived from the ERS 2
965 and ENVISAT radar altimetry missions. *Remote Sensing of Environment*, 114,
966 10, 2160-2181.

967 Schmidt, R., Flechtner, F., Meyer, U., Neumayer, K. -H., Dahle, Ch., Koenig, R., et al.
968 (2008). Hydrological signals observed by the GRACE satellites. *Surveys in*
969 *Geophysics*, 29, 319–334. doi:10.1007/s10712-008-9033-3.

970 Seyler, P., Boaventura, G.R., 2003. Distribution and partition of trace metals in the
971 Amazon basin. *Hydrol. Process.* 17, 1345–1361.

972 Simard, M., Pinto, N., Fisher, J., Baccini, A., (2011), Mapping forest canopy height
973 globally with spaceborne lidar, *Journal of Geophysical Research*, 116, G04021, 12
974 PP., 2011, doi:10.1029/2011JG001708

975 Shuttleworth, W.J., 1993. Evaporation. In: Maidment, D.R. (Ed.), *Handbook of*
976 *Hydrology*. McGraw-Hill, New York.

977 Sun, G., Ranson, K.J., Kharuk, V.I., Kovacs. K. 2003. Validation of surface height from
978 shuttle radar topography mission using shuttle laser altimeter. *Remote Sensing of*
979 *Environment* 88, 401–411 pp.

980 Tapley, B. D., Bettadpur, S., Ries, J. C., Thompson, P. F., & Watkins, M. (2004).
981 GRACE measurements of mass variability in the Earth system. *Science*, 305,
982 503–505.

983 Tian, Y.; Peters-Lidard, C. D. (2010) A global map of uncertainties in satellite-based
984 precipitation measurements. *Geophys. Res. Letters* 37, L24407,
985 doi:10.1029/2010GL046008.

986 Todini, E. (2007). A mass conservative and water storage consistent variable parameter
987 Muskingum-Cunge approach, *Hydrol. Earth Syst. Sci.*, 11, 1645-1659,
988 doi:10.5194/hess-11-1645-2007.

989 Tomasella, J.; Borma, L. S.; Marengo, J. A.; Rodriguez, D. A.; Cuartas, L. A. Nobre, C.
990 A.; Prado, M. C. R. 2010 The droughts of 1996–1997 and 2004–2005 in
991 Amazonia: hydrological response in the river main-stem. *Hydrol. Process.*

992 Trigg, M.A., Wilson, M.D., Bates, P.D., Horritt, M.S., Alsdorf, D.E., Forsberg B.R.,
993 Vega, M.C. 2009. Amazon flood wave hydraulics. *Journal of Hydrology*, 374, 92–
994 105.

995 Trigg, M. A., P. D. D. Bates, M. D. Wilson, G. J.-P. Schumann, and C. A. Baugh
996 (2012), Floodplain channel morphology and networks of the middle Amazon
997 River, *Water Resour. Res.*, doi:10.1029/2012WR011888, in press.

998 Wilson, W., P. Bates, D. Alsdorf, B. Forsberg, M. Horritt, J. Melack, F. Frappart, and J.
999 Famiglietti (2007), Modeling large-scale inundation of Amazonian seasonally
1000 flooded wetlands, *Geophys. Res. Lett.*, 34, L15404, doi:10.1029/2007GL030156.

1001 Yapo, P. O.; Gupta, H. V.; Sorooshian, S. 1998 Multi-objective global optimization for
1002 hydrologic models. *Journal of Hydrology*, 204, 83-97 pp.

1003 Yamazaki, D., S. Kanae, H. Kim, and T. Oki (2011), A physically based description of
1004 floodplain inundation dynamics in a global river routing model, *Water Resour.*
1005 *Res.*, 47, W04501, doi:10.1029/2010WR009726.

1006 Yamazaki, D., H. Lee, D.E. Alsdorf, E. Dutra, H. Kim, S. Kanae, T. Oki (2012),
1007 Analysis of the water level dynamics simulated by a global river model: a case

1008 study in the Amazon River, Water Resources Research,
1009 doi:10.1029/2012WR011869[http://www.agu.org/pubs/crossref/pip/2012WR0118](http://www.agu.org/pubs/crossref/pip/2012WR011869.shtml)
1010 69.shtml
1011 Yamazaki, D., C. Baugh, P. D. Bates, S. Kanae, D. E. Alsdorf, and T. Oki (2012),
1012 Adjustment of a spaceborne DEM for use in floodplain hydrodynamic modelling.
1013 J. Hydrol., 436-437, 81-91, doi:10.1016/j.jhydrol.2012.02.045

1014 **Tables**

1015

1016 Table 1 – Geomorphologic equations developed to estimate river geometric parameters
 1017 in computational cross sections: river width, B [m]; maximum water depth, H [m];
 1018 upstream drainage area Ad [km²].

| River Sub-Basin | River width [m] | Maximum water depth [m] |
|--------------------------------|--------------------|--|
| Tapajós and Xingu | $B=0.35.Ad^{0.62}$ | $H=1.91.Ad^{0.15}$ |
| Purus and Juruá | $B=3.75.Ad^{0.36}$ | $H=2.35.Ad^{0.16}$ |
| Madeira | $B=1.30.Ad^{0.46}$ | $H=1.25.Ad^{0.20}$ |
| Negro and Japurá | $B=0.41.Ad^{0.63}$ | $H=1.26.Ad^{0.20}$ |
| Solimões | $B=0.80.Ad^{0.53}$ | $H=1.43.Ad^{0.19}$ |
| Solimões/Amazon main stream | | $H=22$ $Ad < 400000$ km ² |
| | $B=1.20.Ad^{0.54}$ | $H=20.86+2.86E-06.Ad$ $Ad < 2150000$ km ² |
| | | $H=-1.04+1.30E-05.Ad$ $Ad > 2150000$ km ² |

1019

1020 Table 2 – Discharge model performance statistics Nash and Suttcliffe index (ENS) and
 1021 delay index (DI) in days at gauging stations presented in Fig. 1 for simulations using
 1022 hydrodynamic model with(out) floodplain – HDf (HDn) and Muskingum Cunge model
 1023 with(out) floodplain – MCf (MCn).

| Gauge | River | ENS | | | | DI (days) | | | |
|-------|----------|-------|------|-------|-------|-------------|-----|-----|-----|
| | | HDf | MCf | HDn | MCn | HDf | MCf | HDn | MCn |
| Jap | Japura | 0.21 | 0.22 | 0.11 | 0.1 | -21 | -21 | -27 | -27 |
| Mou | Negro | 0.65 | 0.66 | 0.49 | 0.45 | 5 | -6 | -24 | -26 |
| Pur | Purus | 0.91 | 0.74 | 0.66 | 0.61 | -6 | -18 | -22 | -24 |
| Faz | Madeira | 0.92 | 0.88 | 0.63 | 0.54 | 8 | -4 | -26 | -29 |
| Ita | Tapajós | 0.87 | 0.84 | 0.85 | 0.85 | -2 | 9 | -5 | -5 |
| Tam | Solimões | 0.74 | 0.67 | 0.21 | 0.04 | -3 | -11 | -35 | -39 |
| Man | Solimões | 0.77 | 0.31 | -1.15 | -1.44 | -10 | -36 | -71 | -76 |
| Obd | Amazon | 0.89 | 0.72 | -0.37 | -0.51 | -11 | -24 | -60 | -64 |

1024

1025 **Figure captions**

1026

1027 Figure 1 – (a) Amazon River basin with its main tributaries, international limits, relief
1028 from SRTM DEM and some of the validation sites. Symbols for the location of the
1029 validation sites presented in Figures 3 and 5 are as following: black circles for the
1030 gauge-based discharge series, grey rectangles for the gauge-based water level series,
1031 and black crosses for the altimetry-based water level series. Amazon River basin
1032 discretization into (b) catchments and (c) river reaches simulated using the Muskingum
1033 Cunge (MC) and hydrodynamic (HD) models.

1034

1035 Figure 2 – Validation of daily discharge derived from MGB-IPH model against stream
1036 gauge observations. Spatial distribution, probability (pdf) and cumulative (cdf)
1037 distribution functions of model performance statistics (a) Nash and Sutcliffe Index
1038 (*ENS*), (b) delay index (*DI*) and (c) volume error (ΔV) and (d) relation between
1039 upstream drainage area and model performance statistics.

1040

1041 Figure 3 - Observed (blue line) and simulated (red line) daily discharge in (a) Japurá
1042 River (Jap), (b) lower Negro River at Moura (Mou), (c) lower Purus River (Pur), (d)
1043 lower Madeira River at Fazenda Vista Alegre (Faz), (e) lower Tapajós River at Itaituba
1044 (Ita), (f) Solimões River at Tamshiyacu (Tam), (g) Solimões River close to confluence
1045 with Negro at Manacapuru (Man), and (h) Amazon River at Obidos (Obd). Sites are
1046 indicated in Fig. 1.

1047

1048 Figure 4 - Observed (blue line) and simulated (red line) anomalies of monthly
1049 discharges in the Amazon River at Obidos (Obd).

1050

1051 Figure 5 – Validation of daily water levels derived from MGB-IPH model against
1052 stream gauge observations (squares) and ENVISAT satellite altimetry data (circles).
1053 Spatial distribution of model performance statistics Nash and Sutcliffe Index (*ENS*),
1054 Pearson correlation coefficient (*R*), amplitude error (*A'*),\ delay index (*DI*) and bias
1055 (*BIAS*).

1056

1057 Figure 6 - Simulated (red line) and observed daily water levels from stream gauges
1058 (blue line) and derived from ENVISAT satellite altimetry data (blue points) at (a)
1059 Solimões River (Sol), (b) upper Purus River basin at Acre River in Rio Branco (RBra),
1060 (c) lower Tapajós River at Itaituba (Ita), (d) lower Juruá River (Jur) (e) lower Branco
1061 River (Bra), (f) Amazon River at Óbidos (Obd). Sites are indicated in Fig. 1.

1062

1063 Figure 7 – Seasonal variation of inundation extent derived from MGB-IPH model and
1064 remote sensing estimates from Papa et al. (2010). Average values for DJF, MAM, JJA
1065 and SON seasons were computed for the 1999 to 2004 period.

1066

1067 Figure 8 – Monthly flooded area derived from MGB-IPH model (red dashed line) and
1068 remote sensing estimates from Papa et al. (2010) (blue line) at central Amazon (8°S
1069 70°W to 2°N 60°W), Bolivian Amazon (18°S 70°W to 10°S 60°W), Peruvian Amazon
1070 (12°S 78°W to 0°S 70°W), lower Amazon (8°S 60°W to 0°S 50°W), and Amazon River
1071 basin. Regions are presented in Fig. 7.

1072

1073 Figure 9 – Validation of monthly Terrestrial Water Storage (TWS) derived from MGB-
1074 IPH model against GRACE estimates (2003-2009). (a) Spatial distribution of Nash and

1075 Sutcliffe Index (ENS), amplitude error (A'), observed amplitude (A_{obs}). Monthly time
1076 series of TWS derived from MGB-IPH model (black) and 6 GRACE solutions (grey) in
1077 (b) Lower Negro River Basin ($4^\circ \times 4^\circ$ pixel centered in $62^\circ W$, $2^\circ S$), (c) Upper Tapajós
1078 River Basin ($58^\circ W$, $10^\circ S$) and (d) Amazon River Basin. Statistics are presented for CSR
1079 solution with 400 km Gaussian filter.

1080

1081 Figure 10 – Sensitivity analysis: Climatology of discharge at Óbidos (Obd), water depth
1082 at Manacapuru (Man) and total flooded area derived from simulations using perturbed
1083 values of river width, manning coefficient, river bottom level and precipitation.

1084

1085 Figure 11 – Sensitivity analysis: Climatology of discharge at Óbidos (Obd), water depth
1086 at Manacapuru (Man) and total flooded area derived from simulations using perturbed
1087 values of flooded area and maximum soil storage.

1088

1089 Figure 12 – Water balance of the Amazon River basin. Monthly (left) and
1090 climatological (right) values of mean precipitation (black), evapotranspiration (red) and
1091 discharge close to the outlet at Óbidos (blue). Continuous lines (points) show simulation
1092 results (not) considering the influence of flood extent variability on evapotranspiration.

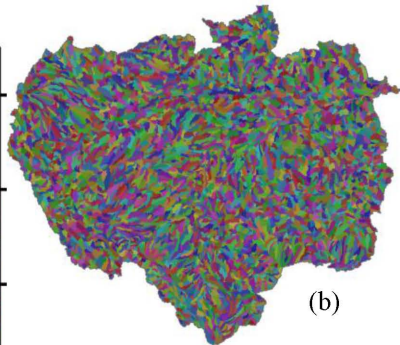
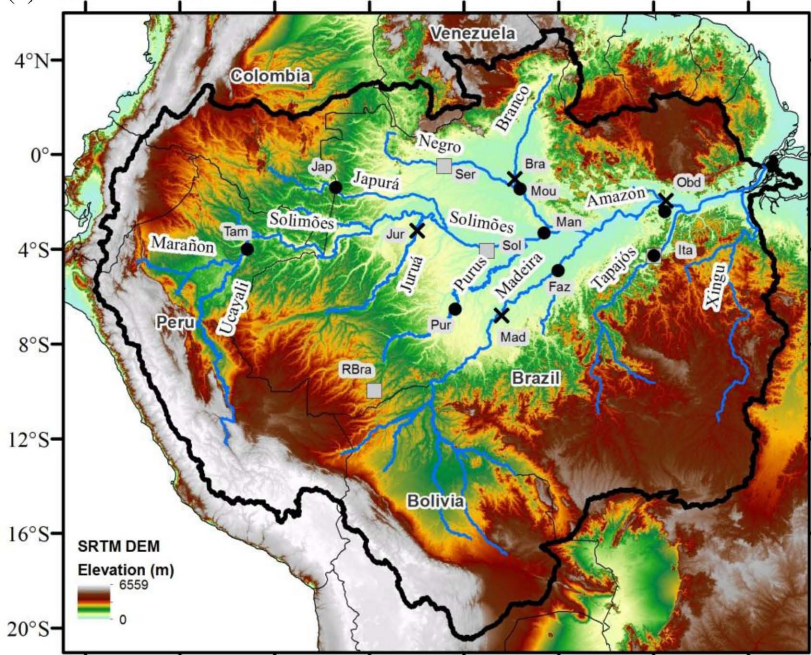
1093

1094 Figure 13 – Fraction of terrestrial water storage divided into surface, soil and ground
1095 waters. (a) Spatial distribution of the fraction of TWS amplitude from each hydrological
1096 compartment. (b) Monthly time series of TWS from surface (blue), soil (red) and
1097 ground (black) waters.

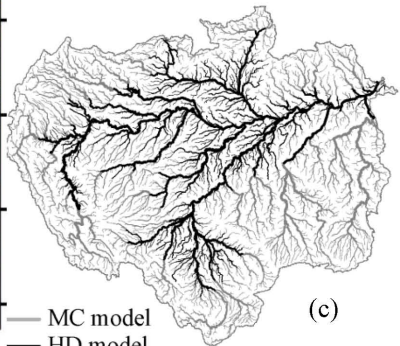
1098

1099 Figure 14 – Observed (black line with dots) and simulated discharges at Óbidos (a) and
1100 Manacapuru (b) sites using hydrodynamic model with floodplains (blue line with dots),
1101 Muskingum Cunge with floodplains (red line), hydrodynamic model without
1102 floodplains (dashed black line) and Muskingum Cunge model without floodplains (grey
1103 line).
1104

(a) 80°W 76°W 72°W 68°W 64°W 60°W 56°W 52°W



(b)



(c)

Figure 1 – (a) Amazon River basin with its main tributaries, international limits, relief from SRTM DEM and some of the validation sites. Symbols for the location of the validation sites presented in Figures 3 and 5 are as following: black circles for the gauge-based discharge series, grey rectangles for the gauge-based water level series, and black crosses for the altimetry-based water level series. Amazon River basin discretization into (b) catchments and (c) river reaches simulated using the Muskingum Cunge (MC) and hydrodynamic (HD) models.

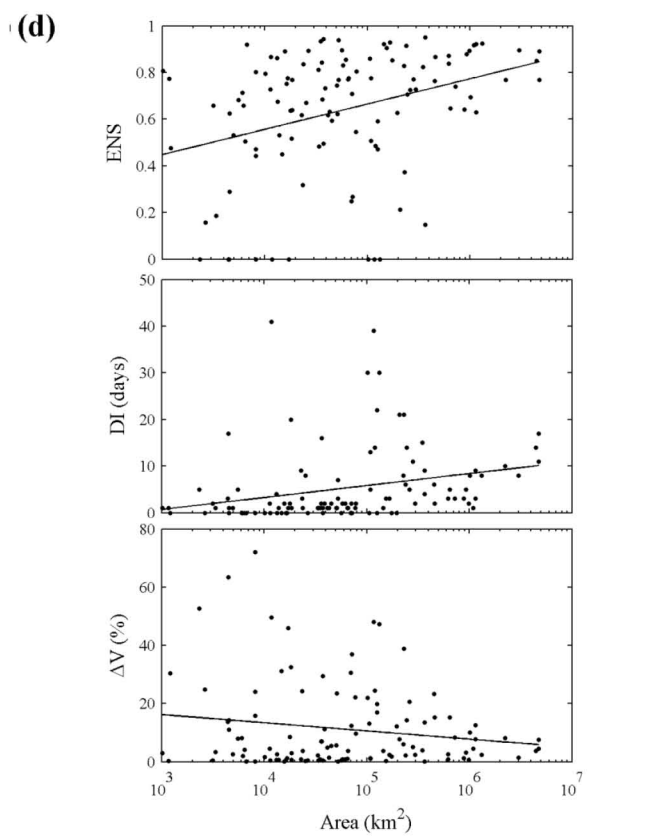
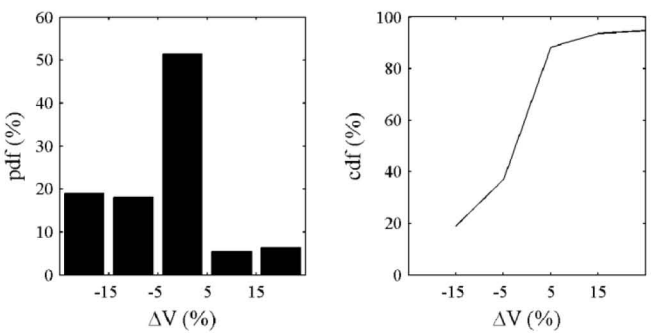
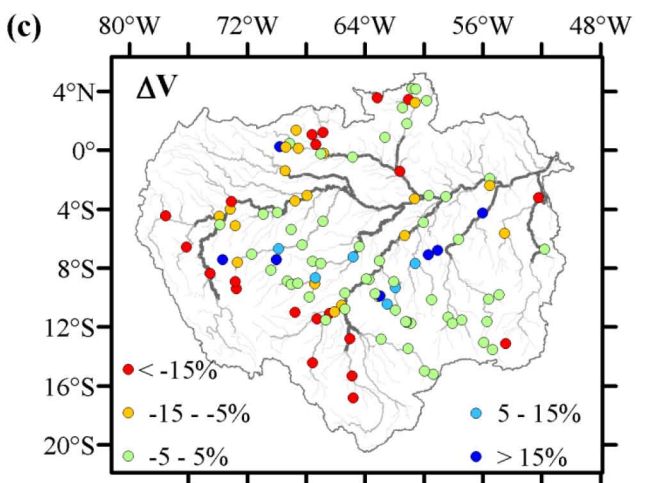
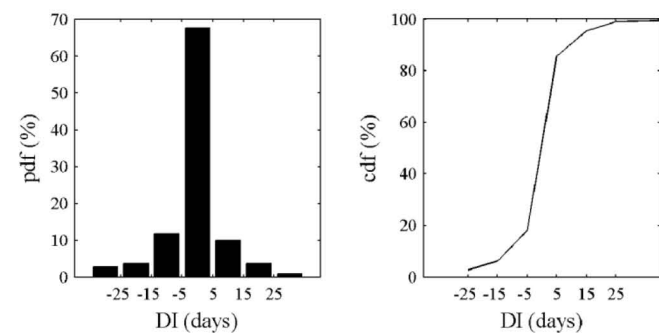
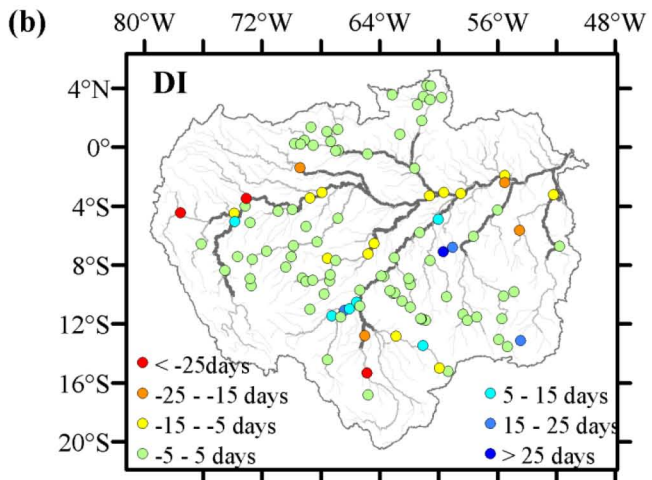
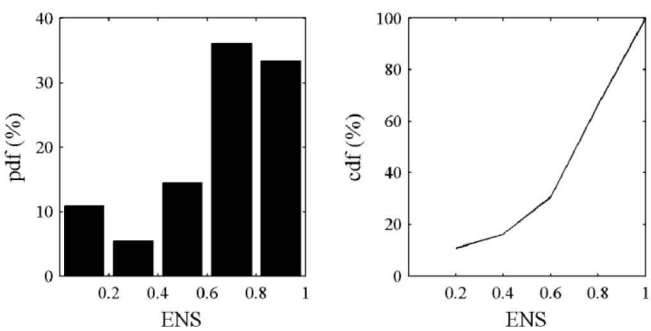
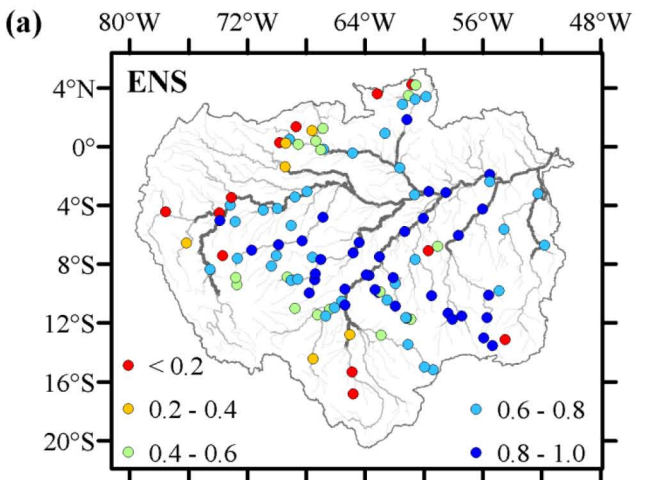
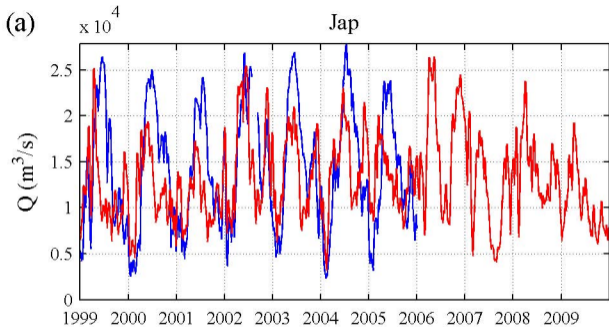


Figure 2 – Validation of daily discharge derived from MGB-IPH model against stream gauge observations. Spatial distribution, probability (pdf) and cumulative (cdf) distribution functions of model performance statistics (a) Nash and Sutcliffe Index (*ENS*), (b) delay index (*DI*) and (c) volume error (ΔV) and (d) relation between upstream drainage area and model performance statistics.

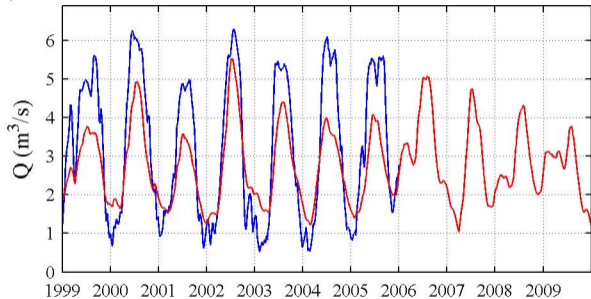


ENS = 0.21, ENSlog = 0.33, DI = -21 days, $\Delta V = -8\%$

(b)

$\times 10^4$

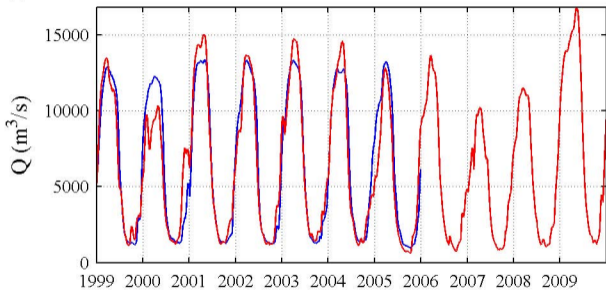
Mou



ENS = 0.65, ENSlog = 0.68, DI = 5 days, $\Delta V = -15\%$

(c)

Pur

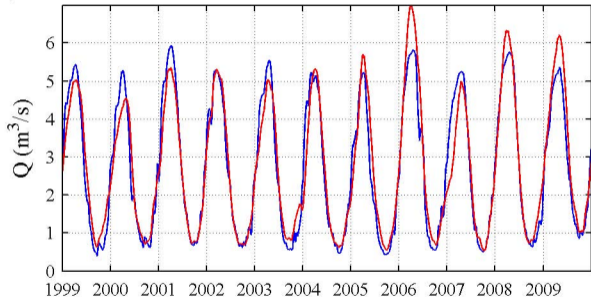


ENS = 0.91, ENSlog = 0.92, DI = -6 days, $\Delta V = -2\%$

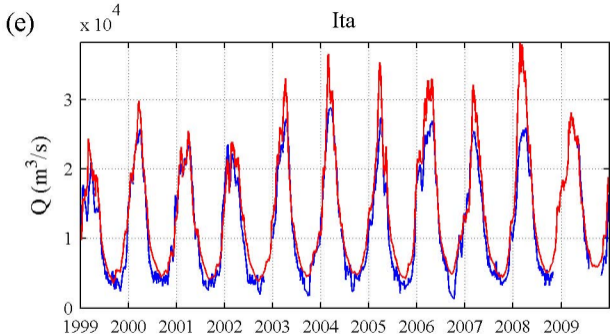
(d)

$\times 10^4$

Faz



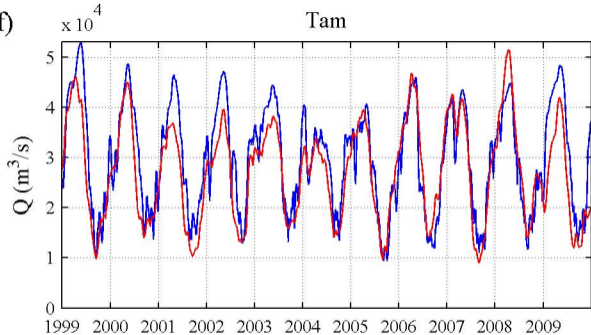
ENS = 0.92, ENSlog = 0.93, DI = 8 days, $\Delta V = 2 \%$



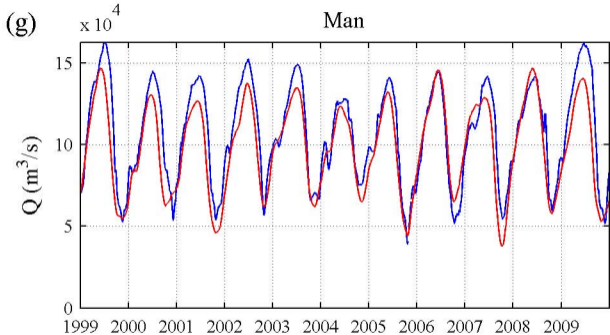
ENS = 0.87, ENSlog = 0.84, DI = -2 days, $\Delta V = 15\%$

(f)

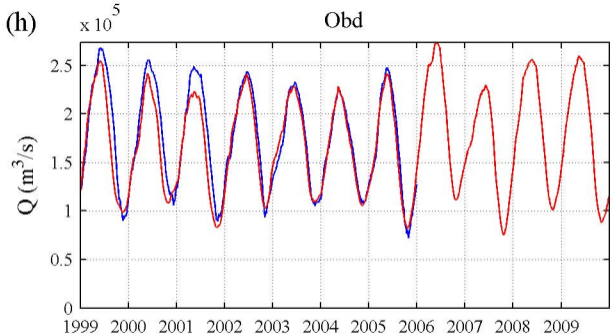
Tam



ENS = 0.74, ENSlog = 0.73, DI = -3 days, $\Delta V = -8 \%$



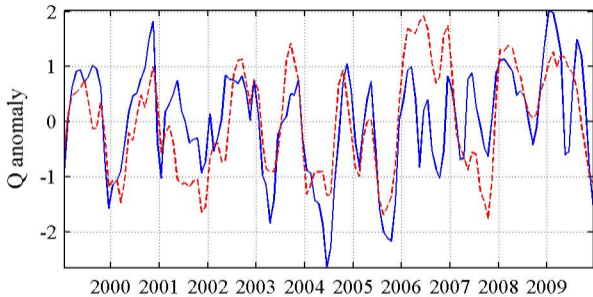
ENS = 0.77, ENSlog = 0.76, DI = -10 days, $\Delta V = -8 \%$



ENS = 0.89, ENSlog = 0.89, DI = -11 days, $\Delta V = -5\%$

Figure 3 - Observed (blue line) and simulated (red line) daily discharge in (a) Japurá River (Jap), (b) lower Negro River at Moura (Mou), (c) lower Purus River (Pur), (d) lower Madeira River at Fazenda Vista Alegre (Faz), (e) lower Tapajós River at Itaituba (Ita), (f) Solimões River at Tamshiyacu (Tam), (g) Solimões River close to confluence with Negro at Manacapuru (Man), and (h) Amazon River at Obidos (Obd). Sites are indicated in Fig. 1.

Obd



$R = 0.63$

Figure 4 - Observed (blue line) and simulated (red line) anomalies of monthly discharges in the Amazon River at Obidos (Obd).

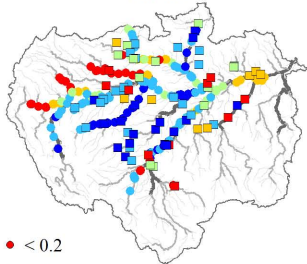
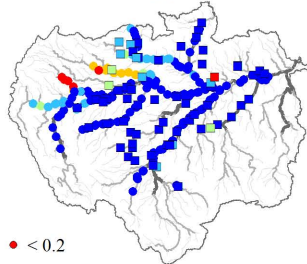
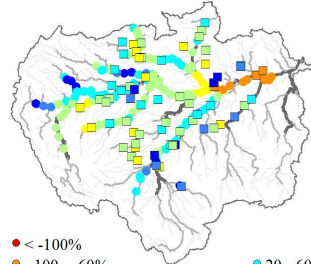
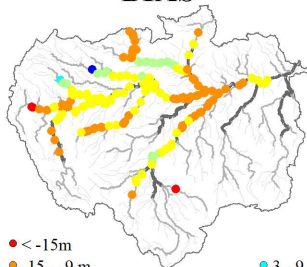
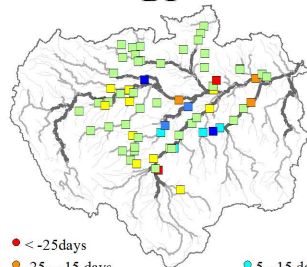
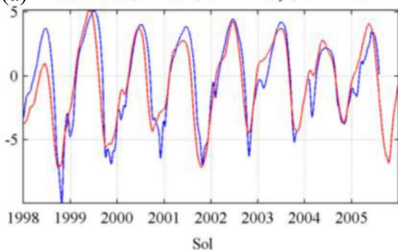
ENS**R****A'****BIAS****DI**

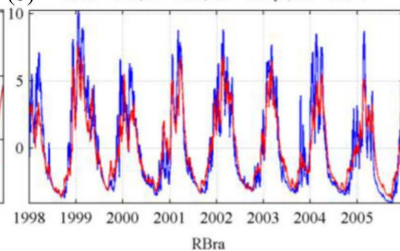
Figure 5 – Validation of daily water levels derived from MGB-IPH model against stream gauge observations (squares) and ENVISAT satellite altimetry data (circles). Spatial distribution of model performance statistics Nash and Sutcliffe Index (*ENS*), Pearson correlation coefficient (*R*), amplitude error (*A'*), delay index (*DI*) and bias (*BIAS*).

Water level [m]

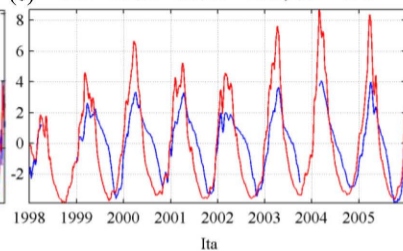
(a) ENS = 0.80, R = 0.89, DI = -15 days, A' = -7 %



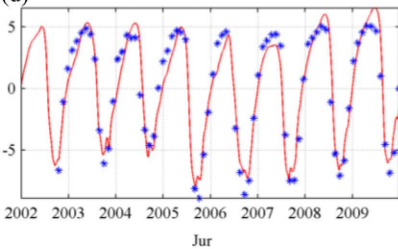
(b) ENS = 0.85, R = 0.93, DI = 0 days, A' = -20 %



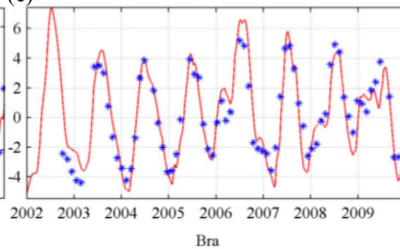
(c) ENS = 0.05, R = 0.82, DI = -24 days, A' = 48 %



(d) ENS = 0.91, R = 0.96, A' = 0 %, BIAS = -4.9 m



(e) ENS = 0.83, R = 0.92, A' = 0 %, BIAS = -10.1 m



(f) ENS = 0.31, R = 0.90, A' = -80 %, BIAS = -8.8 m

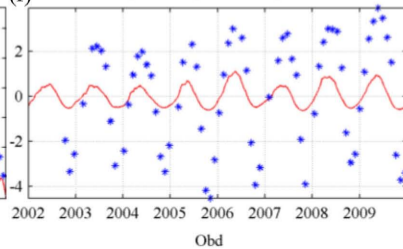
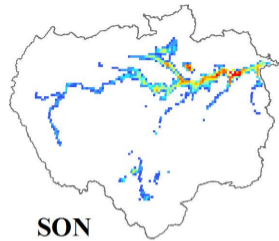
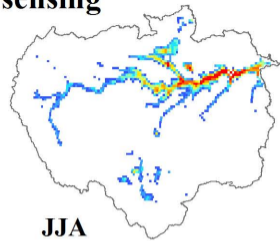
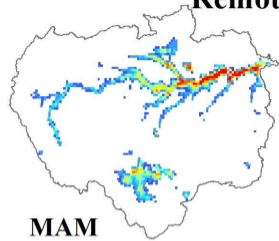
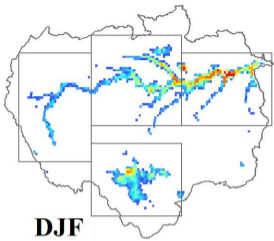


Figure 6 - Simulated (red line) and observed daily water levels from stream gauges (blue line) and derived from ENVISAT satellite altimetry data (blue points) at (a) Solimões River (Sol), (b) upper Purus River basin at Acre River in Rio Branco (RBra), (c) lower Tapajós River at Itaituba (Ita), (d) lower Juruá River (Jur) (e) lower Branco River (Bra), (f) Amazon River at Óbidos (Obd). Sites are indicated in Fig. 1.

Remote sensing



Model

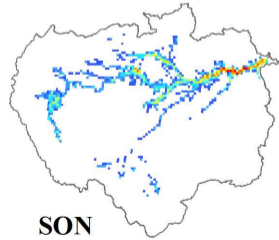
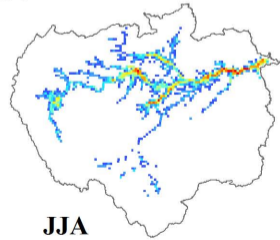
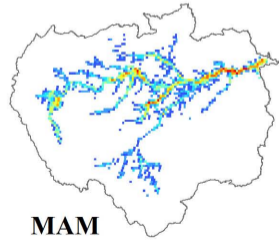
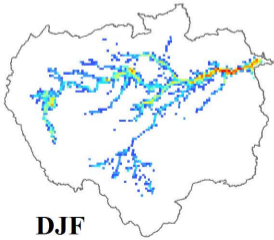
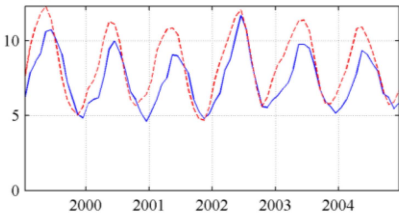


Figure 7 – Seasonal variation of inundation extent derived from MGB-IPH model and remote sensing estimates from Papa et al. (2010). Average values for DJF, MAM, JJA and SON seasons were computed for the 1999 to 2004 period.

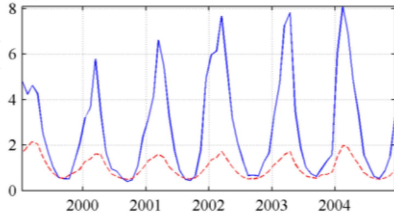
Flooded area [km²]

$\times 10^4$ ENS = 0.26, R = 0.85, A' = 12 %, BIAS = 14 %



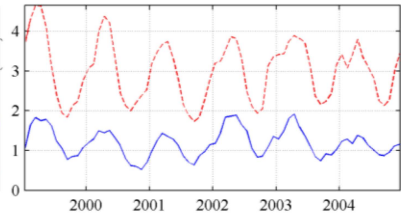
Central Amazon

$\times 10^4$ ENS = -0.28, R = 0.89, A' = -79 %, BIAS = -63 %



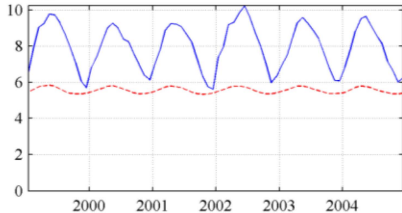
Bolivian Amazon

$\times 10^4$ ENS = -27.77, R = 0.84, A' = 102 %, BIAS = 151 %



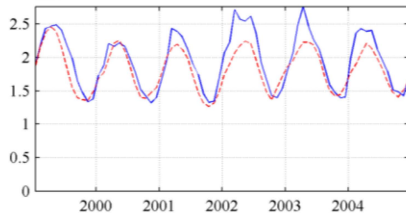
Peruvian Amazon

$\times 10^4$ ENS = -3.39, R = 0.90, A' = -88 %, BIAS = -30 %



Lower Amazon

$\times 10^5$ ENS = 0.71, R = 0.92, A' = -26 %, BIAS = -7 %

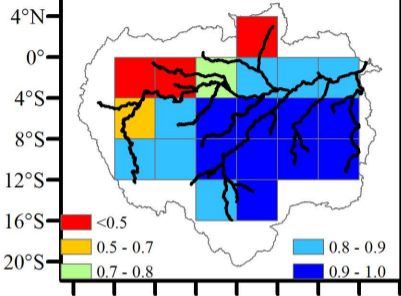


Amazon River Basin

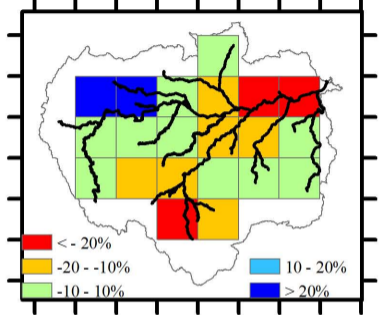
Figure 8 – Monthly flooded area derived from MGB-IPH model (red dashed line) and remote sensing estimates from Papa et al. (2010) (blue line) at central Amazon (8°S 70°W to 2°N 60°W), Bolivian Amazon (18°S 70°W to 10°S 60°W), Peruvian Amazon (12°S 78°W to 0°S 70°W), lower Amazon (8°S 60°W to 0°S 50°W), and Amazon River basin. Regions are presented in Fig. 7.

(a)**ENS**

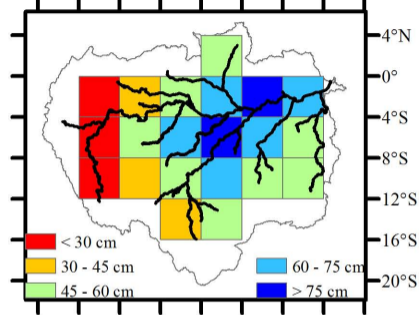
80°W 72°W 64°W 56°W 48°W

**A'**

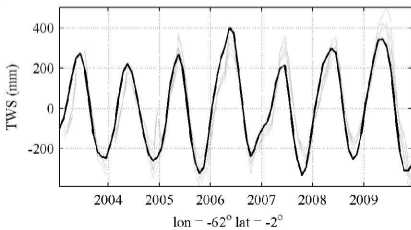
80°W 72°W 64°W 56°W 48°W

**Aobs**

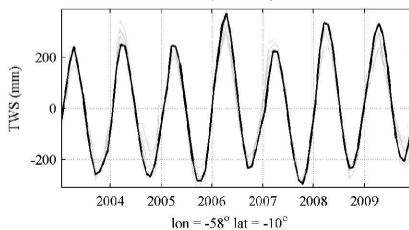
80°W 72°W 64°W 56°W 48°W

**(b)**

ENS = 0.86, R = 0.93, A' = -17%

**(c)**

ENS = 0.96, R = 0.98, A' = 4%

**(d)**

ENS = 0.93, R = 0.97, A' = 12%

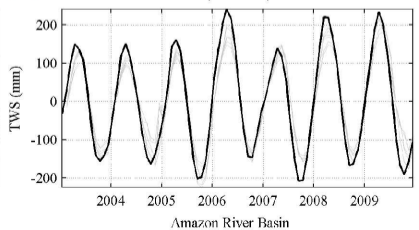


Figure 9 – Validation of monthly Terrestrial Water Storage (TWS) derived from MGB-IPH model against GRACE estimates (2003-2009). (a) Spatial distribution of Nash and Sutcliffe Index (ENS), amplitude error (A'), observed amplitude (A_{obs}). Monthly time series of TWS derived from MGB-IPH model (black) and 6 GRACE solutions (grey) in (b) Lower Negro River Basin ($4^{\circ} \times 4^{\circ}$ pixel centered in $62^{\circ}W$, $2^{\circ}S$), (c) Upper Tapajós River Basin ($58^{\circ}W$, $10^{\circ}S$) and (d) Amazon River Basin. Statistics are presented for CSR solution with 400 km Gaussian filter.

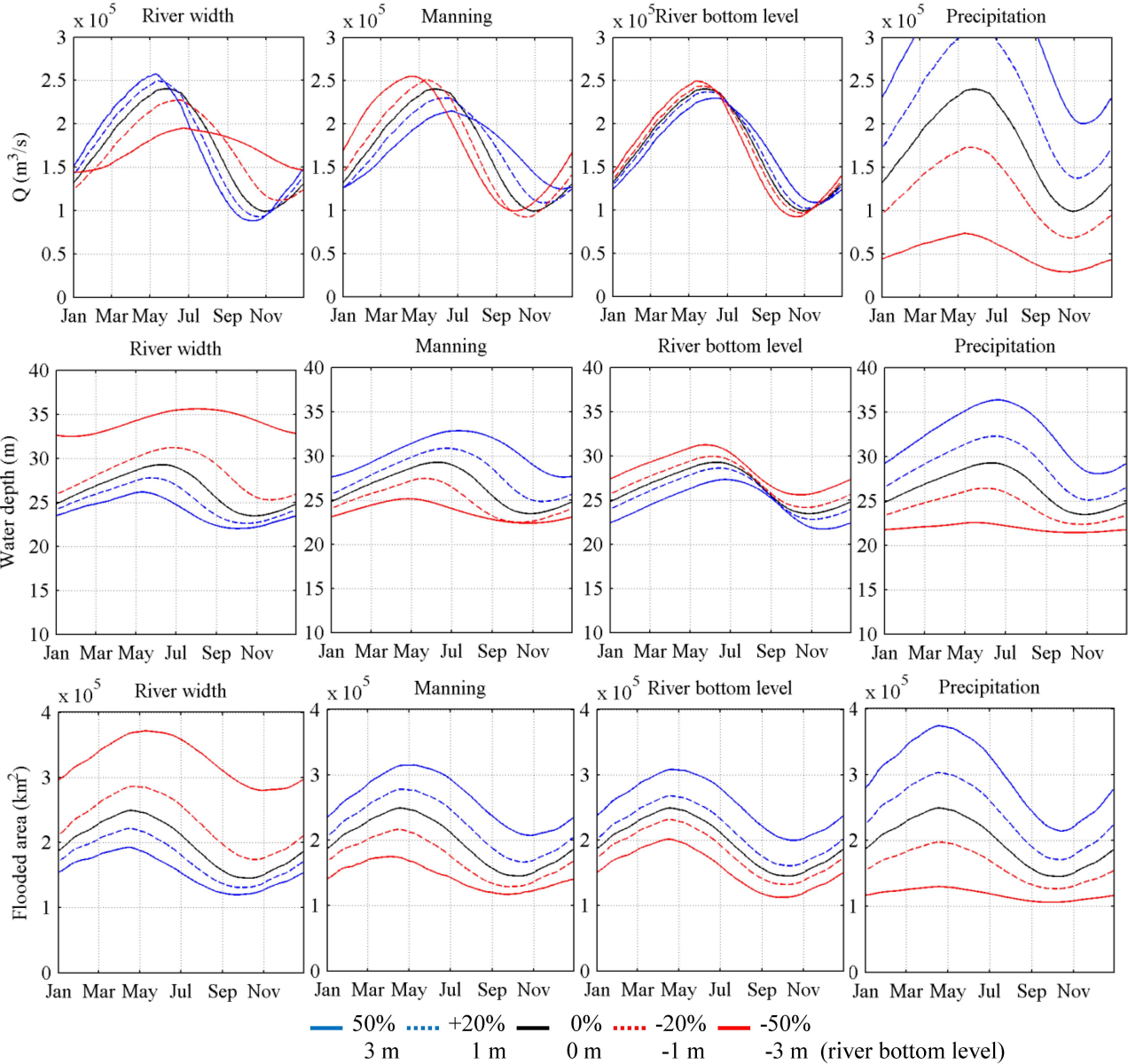
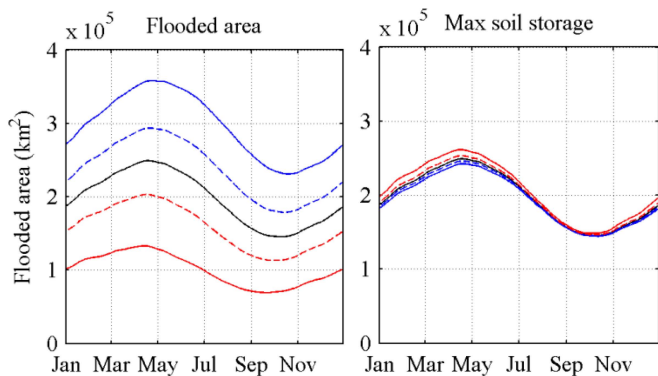
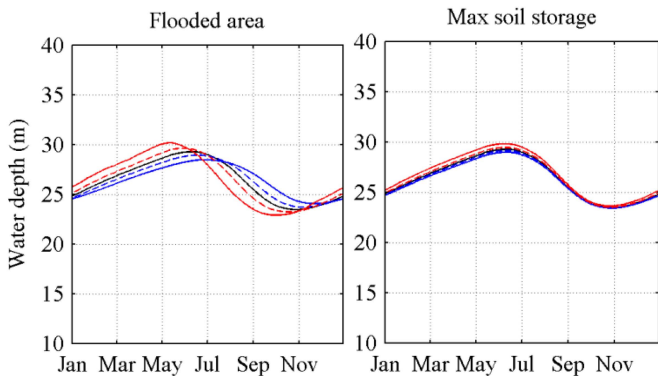
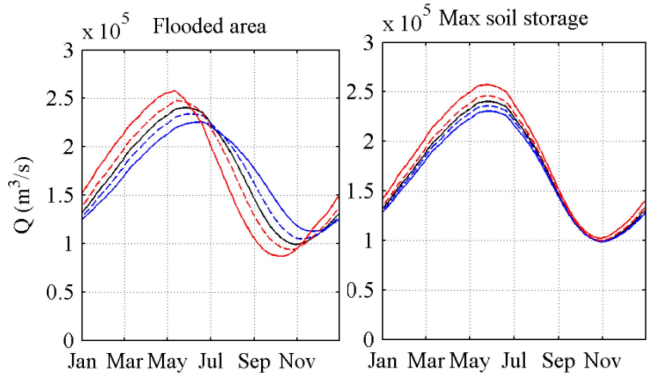


Figure 10 – Sensitivity analysis: Climatology of discharge at Óbidos (Obd), water depth at Manacapuru (Man) and total flooded area derived from simulations using perturbed values of river width, manning coefficient, river bottom level and precipitation.



— 50% - - - +20% — 0% - - - -20% — -50%

Figure 11 – Sensitivity analysis: Climatology of discharge at Óbidos (Obd), water depth at Manacapuru (Man) and total flooded area derived from simulations using perturbed values of flooded area and maximum soil storage.

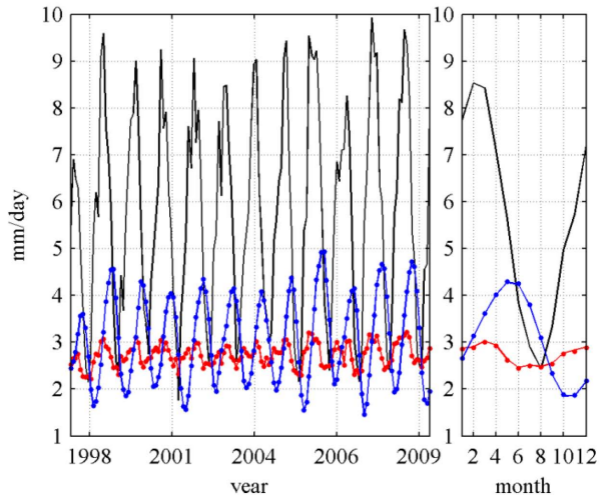
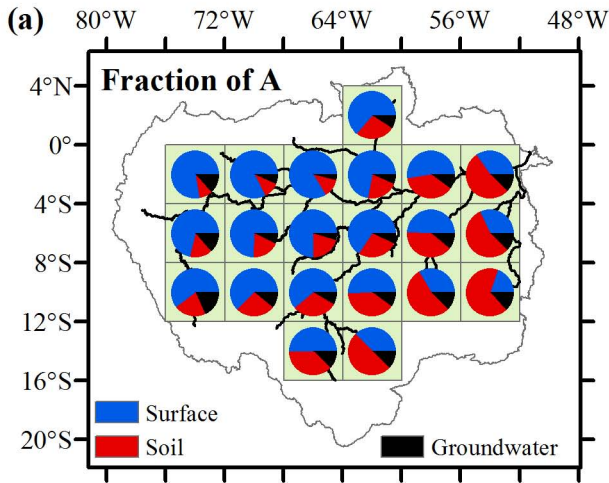


Figure 12 – Water balance of the Amazon River basin. Monthly (left) and climatological (right) values of mean precipitation (black), evapotranspiration (red) and discharge close to the outlet at Óbidos (blue). Continuous lines (points) show simulation results (not) considering the influence of flood extent variability on evapotranspiration.



surface = 56 %, soil = 36 %, groundwater = 8 %

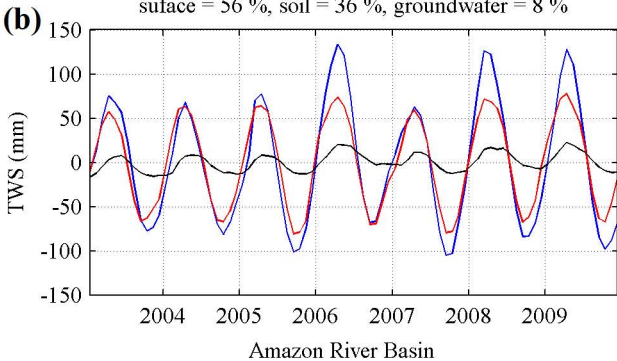
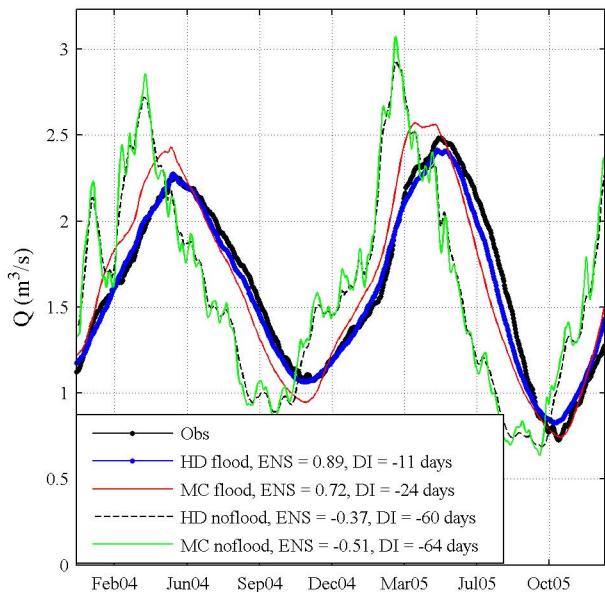


Figure 13 – Fraction of terrestrial water storage divided into surface, soil and ground waters. (a) Spatial distribution of the fraction of TWS amplitude from each hydrological compartment. (b) Monthly time series of TWS from surface (blue), soil (red) and ground (black) waters.

(a) $\times 10^5$ Óbidos (Obd) - Amazon River



(b) $\times 10^5$ Manacapuru (Man) - Solimoes River

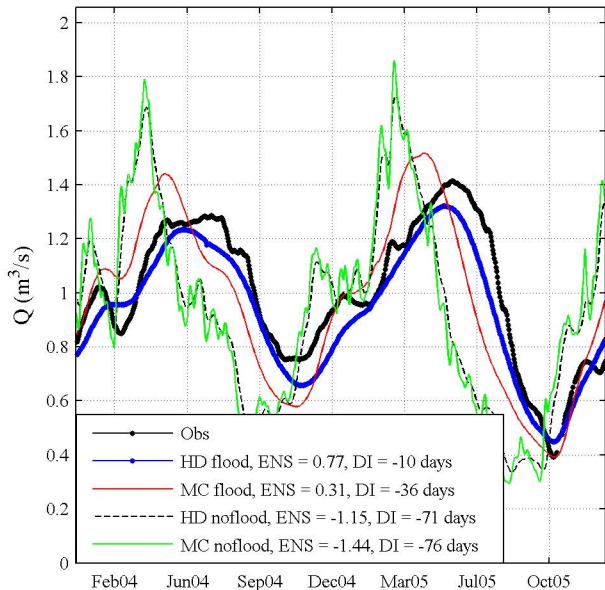


Figure 14 – Observed (black line with dots) and simulated discharges at Óbidos (a) and Manacapuru (b) sites using hydrodynamic model with floodplains (blue line with dots), Muskingum Cunge with floodplains (red line), hydrodynamic model without floodplains (dashed black line) and Muskingum Cunge model without floodplains (grey line).